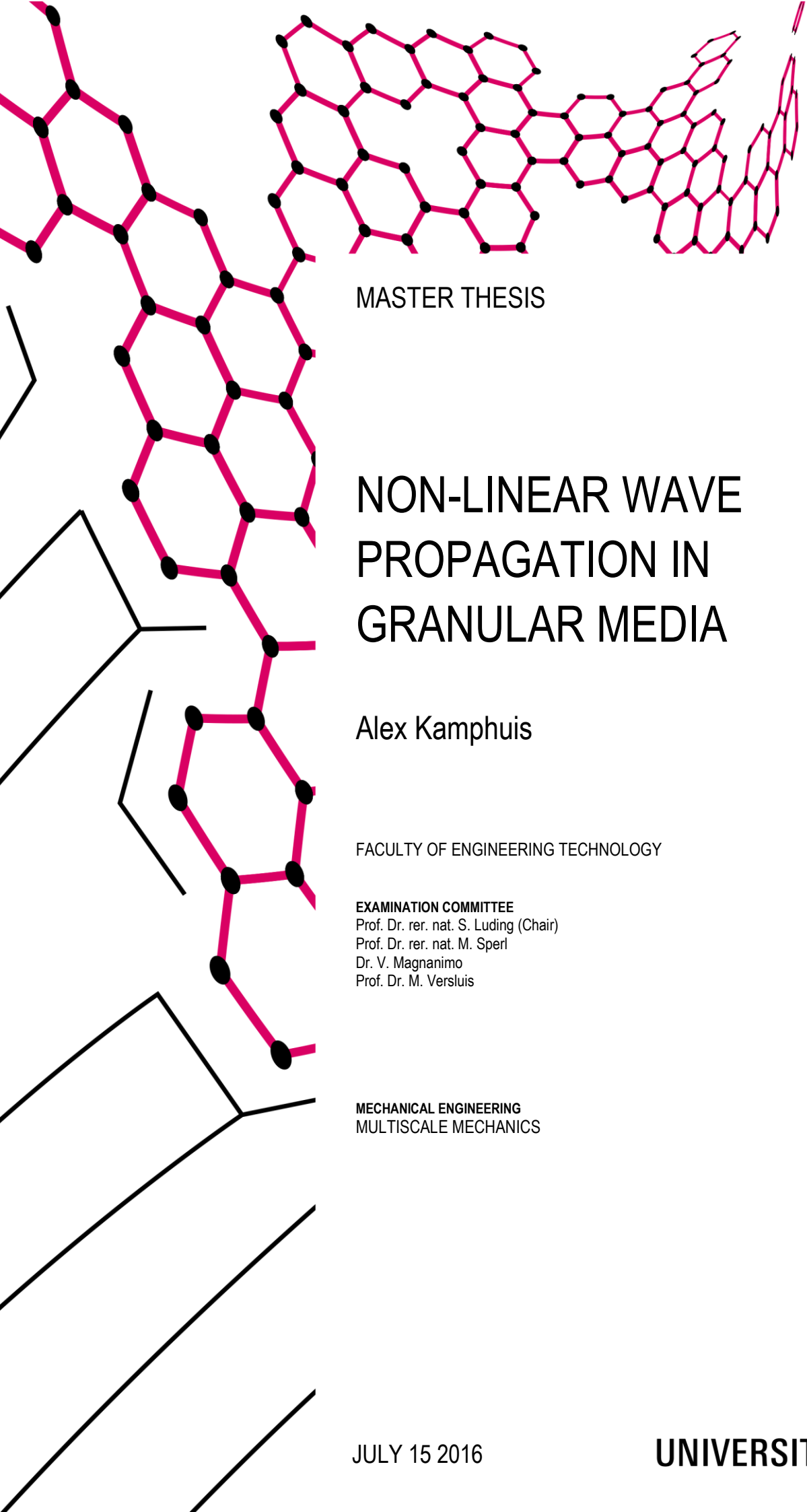

MASTER THESIS

NON-LINEAR WAVE PROPAGATION IN GRANULAR MEDIA

Alex Kamphuis

FACULTY OF ENGINEERING TECHNOLOGY

EXAMINATION COMMITTEE
Prof. Dr. rer. nat. S. Luding (Chair)
Prof. Dr. rer. nat. M. Sperl
Dr. V. Magnanimo
Prof. Dr. M. Versluis

MECHANICAL ENGINEERING
MULTISCALE MECHANICS

JULY 15 2016

UNIVERSITY OF TWENTE.

Summary

A collection of macroscopic particles with mainly repulsive inter-particle forces - like dry sand - is called a granular medium. Systems like these can show phenomena different from traditional solids, liquids and gases such as (un)jamming, force chains and non-linear pressure wave propagation.

"Matter and energy seem granular in structure, and so does 'life', but not so mind."

Erwin Schrödinger, 1956

Nesterenko [1] showed that a granular system can support non-linear pressure waves and the same was later shown in simulation [2, 3] and experimentally [4]. The non-linear behaviour is only predicted for sufficiently high wave amplitudes and sufficiently small confining pressures leading to believe that in the limit of zero confining pressure (which is approximately possible without gravity) all mechanical energy is transported non-linearly (dubbed 'sonic vacuum' by Nesterenko).

The cause of this non-linear behaviour poses serious limitations on simplifications that can be made to granular systems in order to study their behaviour. The aim of this work is therefore to study this non-linear behaviour and the influence of such simplifications and to provide a toolset for future study.

Firstly molecular dynamics simulations (using a newly developed software package) have been used to find whether non-linear wave propagation can be witnessed using simple force laws in one dimension. Using two different contact models (one linear and one Hertzian (non-linear)) a non-linearity was witnessed, but with a power-law much smaller than theoretically predicted. This suggests that the simulations run are over-simplified and can not directly be used to study non-linear wave propagation.

Secondly a layer of stress birefringent disks and spheres was filmed at 40000 frames per second to watch pressure waves travel through packings with different ratios of numbers of spheres to disks. A $\frac{1}{6}$ power-law relation was found between drop height (a measure for wave amplitude) and propagation speed. No significant differences in the non-linear behaviour was found for different mixtures of spheres and disks, justifying the use of these mixtures in two dimensional wave propagation experiments.

Thirdly, within a larger and ongoing project, many data points have been gathered using newly developed software tools that was used aboard a parabolic (zero gravity) flight. The process of analysis (also using newly developed tools) and comparison to data acquired on ground is progressing; preliminary results show a linear and non-linear regime on ground, and possibly increasing sound speed with wave amplitude during 0g. During some parabolas a much more uniform (than in 1g) was achieved. The data proves the effectiveness of the tools developed and new data shows how to further improve the setup.

Contents

Chapter 1.

Introduction

This report concerns itself with the propagation of mechanical waves in so-called granular media. Before diving into more depth a summary of this knowledge is warranted.

> "If you watch the flowing sand, you might see time itself riding the granules."
>
> *Vera Nazarian, 2008*

1.1. Granular Media

Different definitions exist for granular media. In any case a granular medium contains a multitude of discrete particles. The medium describes the collection, the system, of these particles [5]. An assumption generally made is that particles do not interact with each other on the long range because the interparticle forces exist only where large particles are in direct physical contact [6]. The existing definitions differ in exclusion of certain systems based on the type of forces involved or the size of the particles.

In general repulsive forces must dominate over cohesive ones for a system to behave like a granular system [7]. Materials are not (effectively) cohesive above a certain particle size. As a general rule of thumb the particles must exceed a size of 1 [μm] so that Brownian motion and cohesion are sufficiently small to be disregarded. The upper limit of particle size (on earth) is often found in practical issues for it is increasingly difficult to contain a system of particles as they grow larger. Some remarkable exceptions to this rule are for instance ice shelves, the earth's crust and planetary rings. The latter are better defined as dilute granular media or granular gases [8].

The resulting collection of granular media is rather large, containing sand, cereals, beads and others.

1.1.1. Importance

The widespread occurrence of these media has given rise to an ever growing interest since 1900 as depicted in Figure 1.1. Scientific research on the subject of granulars has developed a solid basis in journals like *Granular Matter*, *Powder Technology* and *Particuology*. However more general journals like *Nature*, *Science* and *Physical Review Letters* have also published plenty on the subject.

Swinney and Rericha noted in 2004 [10] that in the chemical industry the majority of the products involved are granulars rather than liquids. It is therefore remarkable

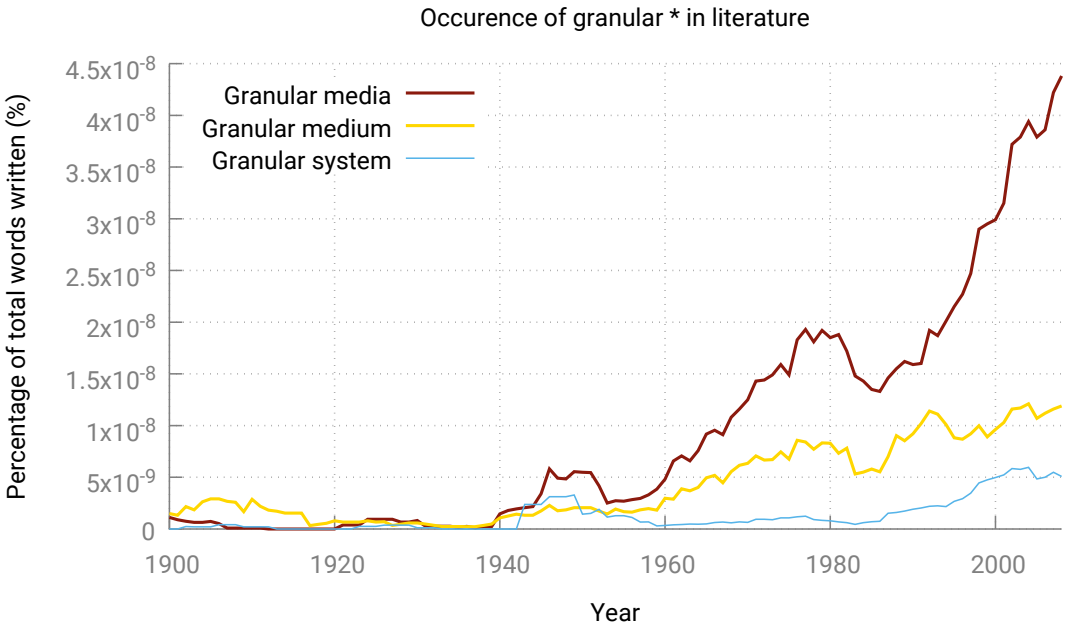

Figure 1.1.: Ngram of several granular related words groups depicting the relative occurrence of these word groups to all other words in Google's database of millions of books [9]. A sharp rise in usage of these words can be seen from 1900 till 2008 (with two drops in 1955 and 1985). Made using the Google's Ngram service (that published no data after 2008.)

that the understanding of these materials is still below that of solids and liquids and the efficiency of processing them is considered below optimal [10]. In 1975 Vaisnys and Pilbeam argued that all attempts to make a complete description of merely the mechanical properties of granular media had so far failed [7]. The understanding of granular media's rich behaviour has since then much increased, but is certainly not yet complete.

1.1.2. Properties

A prime example of a granular medium and its peculiar properties is sand. Sand can be poured producing a flowing behaviour similar to pouring a liquid. However sand can also be piled and resist forces like a solid. From sandcastle building at the beach one may know that dry piles of sand have a limited slope. A slope above a certain angle (called the angle of repose, θ_r) will cause the sand grains to pour down the slope. This behaviour can be seen in Figure 1.2.

Reynolds described in 1885 another phenomenon called dilatancy: the fact that a granular medium must expand (under almost all circumstances) to flow or deform [12]. This can be noticed on the beach; when walking sand around one's foot will dry out

(a) Below repose angle **(b)** Above repose angle

Figure 1.2.: *left:* A pile of mustard seeds with a slope just below the repose angle showing no movement or falling/flowing seeds. *right:* The same pile inclined above the repose angle so that a layer of seeds starts flowing (the blurry layer, due to a long shutter time). Note that below this layer seeds are still non-moving. Both images were originally published in [11].

as pressure on the sand by the foot increases. The deformation caused by this pressure creates space for the water to flow into, leaving upper layer of the sand dry.

One may say that particles must make room for other particles to pass. The amount of room to be made for movement to occur is related to the medium's jamming point. The jamming point is defined as the volume fraction - the ratio between particle and system volume - ϕ at which the medium can no longer flow. Onoda and Liniger [13] showed that without gravity (e.g. in space) the loosest random packing has a packing fraction of $\phi \approx 0.56$ (named the RLP limit) for spheres by immersing them in liquids with varying density. The densest possible packing for spheres is the close-packed hexagonal structure with $\phi \approx 0.74$ which is achieved by decreasing the average interparticle distance with a factor of $(0.74/0.56)^{\frac{1}{3}} \approx 1.1$ [14]. The jamming point ϕ_j should be somewhere between these limits. In Nature, Luding [15] argued that the jamming point should however be considered more of a variable than a fixed point as it may move as the system evolves.

The inhomogeneities in the distribution of particles and forces in granular packings can cause other phenomena such as arching. This can best be compared to a building style often used in churches where the use of a keystone allows to distribute the weight of a roof along the walls to create an empty space below. The same principles apply to sand piles where stress can be transferred from softer to stiffer parts of the packing until a static configuration is formed. This configuration is, however, not typically in isostatic limit [16] (the state to which the system would tend in the absence of friction). Granular media in general show jamming behaviour, meaning that there are several non equilibrium microstates (e.g. the exact particle positions) for a single set of macroscopic parameters (e.g. packing fraction ϕ). It is therefore unlikely that a description of a granular medium using only one macroscopic parameter will ever be complete [17]. Which other parameters to use to create such a complete description is still a topic of research.

The arching phenomenon gives rise to another counterintuitive example encountered in a sand pile. One may expect that in a conical sand pile the pressure due to gravity on the ground is highest directly below the apex, in the centre of the pile. The contrary is however revealed in some experiments that show a local minimum (a dip) in the stress pointing downwards right below the apex. This dip can not be explained by simple isotropic elasticity theory, rendering it invalid in this case. There are other models that can explain the dip, however it has become clear that the existence of a dip depends not only on the sand grains themselves but also on the way the pile was prepared [18]. This history dependence is ever present when dealing with granular media.

A liquid filled container (under gravity) will show a linear relation between pressure and depth. In the case of a granular medium however, packed in a sufficiently high container with rough walls, this is not the case. It can be shown that the friction of the granules with the wall is already enough to carry the weight of the particles on top, causing the pressure at the bottom of the container to be independent of the height of it. This is called the Janssen effect [19].

A way of understanding why the preparation of a granular medium is important is to realize that a collision between particles is highly dissipative. For glass particles the coefficient of restitution can be around 0.81, meaning that at each collision nearly 20 [%] of the energy is lost. For sands and dusts this coefficient can be even lower (around 0.6) [20]. Because there are many collisions between many particles the system quickly loses energy and settles in a static state.

Using stress birefringent materials the inhomogeneity of the force distributions can be made visible as has been done to produce Figure 1.3. Forces clearly concentrate themselves along chains that on first sight have a certain randomness to their orientation. The influence of these force chains on macroscopic properties of the packing has been studied though not yet fully understood [22, 23, 24]. It is however clear from research by Zhang et al. [25] that force chains grow with system size until they reach a maximum at which the average length of the chains remains constant irrespective of system size. Statistical methods are then used to predict a probability that a particle is in a force chain and to relate the coordination number $\bar{z}$ (the amount of other particles a particle touches averaged over all particles) to the length of the chains. The coordination number may then be used to relate to for instance the packing fraction [26].

Another difference between granular matter and traditional states of matter like normal solids, liquids and gases is the transmission of sound (a mechanical- or pressure wave). Whereas in the former cases sound propagates without much distortions (such as attenuation, dispersion and frequency filtering) through the medium the propagation of sound in granular media is qualitatively different [11, 27].

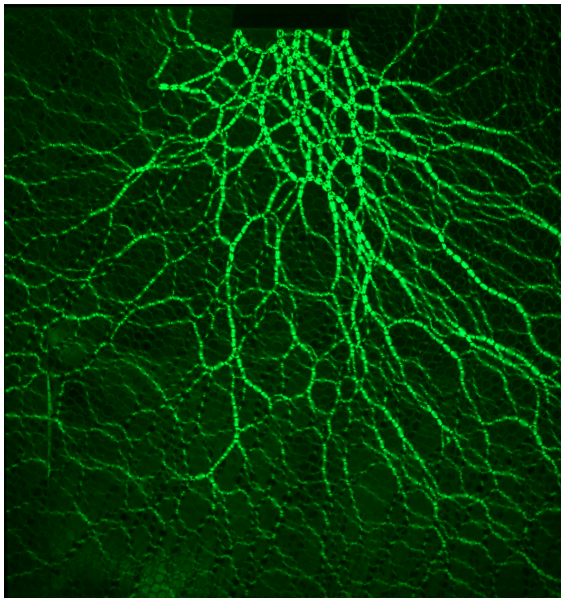

Figure 1.3.: Force chains in a two dimensional (2D) granular packing made visible by shining monochromatic polarized light through stress birefringent particles. The forces start at a square punch (black box on top of image) and travel downwards and sideways to the container walls. Brighter green shows larger stresses. This image was taken from [21] with the authors approval.

1.2. (Sound) Waves

1.2.1. Linear (sound) waves

Sound waves (and many other waves) are governed by the wave equation, which was - according to Weisstein [28] originally found by d'Alambert and later extended to a three dimensional system by Euler. The equation is given by

$$\boldsymbol{\nabla}^2\psi = \frac{1}{c^2}\frac{\partial^2\psi}{\partial t^2}, \tag{1.1}$$

with $\boldsymbol{\nabla}$ the Del operator defined by $\boldsymbol{\nabla} = \sum_{i=1}^{n} \boldsymbol{e}_i \frac{\partial}{\partial x_i}$ in n dimensions, ψ the field governed by the wave equation and t the time. The symbol c is the propagation speed of the wave. The propagation of sound waves, or more general, the propagation of mechanical waves in granular media has been a subject of study. See for instance [29, 30, 31, 32] and references therein for many more. One of the most obvious characteristics of these waves is their propagation speed.

The propagation speed of a sound wave depends on the bulk and shear moduli K and G respectively. In a linear isotropic elastic medium the propagation speed for shear and compressional waves can be found following a conservation of energy argument as discussed next.

Propagation speed of a compressional wave through an elastic medium

Assume a harmonic compressional wave travelling in the x direction:

$$u_x = A\cos\left(\frac{\omega}{c_p}x - \omega t\right) \tag{1.2}$$

with u_x the displacement in the x direction of a point of material, A the amplitude of the wave and ω angular its frequency. The energy in the wave has a kinetic and a potential component that together must be constant. On a per unit volume basis they can be evaluated as

$$\begin{aligned} E_{\text{kin}} &= \frac{1}{2}\rho\left(\frac{\partial u_x}{\partial t}\right)^2 & E_{\text{pot}} &= -\frac{1}{2}M\left(\frac{\partial u_x}{\partial x}\right)^2 \\ &= \frac{1}{2}\rho A^2\omega^2 s(x,t)^2 & &= -\frac{1}{2}M\frac{\omega^2}{c_p^2}A^2 s(x,t)^2 \end{aligned} \tag{1.3}$$

with $s(x,t) = \sin\left(\frac{\omega}{c_p}x - \omega t\right)$ and M the compressional modulus related to the bulk and shear moduli K and G by $M = K + \frac{4}{3}G$. Note the structural similarity of Equation 1.3 to $E_{\text{kin}} = \frac{1}{2}mv^2$ and $E_{\text{pot}} = \frac{1}{2}ku^2$ known as expressions for kinetic and potential energy respectively.

Following from $E_{\text{pot}} + E_{\text{kin}} = \text{constant} \quad \forall x, t$ it can be concluded

$$\begin{aligned} \frac{1}{2}\rho A^2\omega^2 - \frac{1}{2}M\frac{\omega^2}{c_p^2}A^2 &= 0 \\ \rho - M\frac{1}{c_p^2} &= 0 \\ c_p^2 &= \frac{M}{\rho} = \frac{K + \frac{4}{3}G}{\rho}. \end{aligned} \tag{1.4}$$

Propagation speed of a shear wave through an elastic medium

A similar argument can be made for the propagation speed of a shear wave by assuming a shear wave travelling in the x direction described by:

$$u_y = A\cos\left(\frac{\omega}{c_s}x - \omega t\right). \tag{1.5}$$

Its kinetic and potential energy components are then

$$\begin{aligned} E_{\text{kin}} &= \frac{1}{2}\rho\left(\frac{\partial u_y}{\partial t}\right)^2 & E_{\text{pot}} &= \frac{1}{2}G\left(\frac{\partial u_y}{\partial x}\right)^2 \\ &= \frac{1}{2}\rho A^2\omega^2 s(x,t)^2 & &= \frac{1}{2}GA^2\frac{\omega^2}{c_s^2}s(x,t)^2. \end{aligned} \tag{1.6}$$

So that from $E_{\text{pot}} + E_{\text{kin}} = \text{constant} \quad \forall x, t$ follows

$$\frac{1}{2}\rho A^2\omega^2 + \frac{1}{2}GA^2\frac{\omega^2}{c_s^2} = 0 \tag{1.7}$$

$$\rho + G\frac{1}{c_s^2} = 0 \tag{1.8}$$

$$c_s^2 = \frac{G}{\rho}. \tag{1.9}$$

Power law relations

Chotiros and Isakson [32] explain that the moduli K and G are often assumed to be

$$K = \frac{\bar{z}(1-\beta)}{12\pi R}S_n, \qquad G = \frac{\bar{z}(1-\beta)}{20\pi R}\left(S_n + \frac{3}{2}S_t\right), \tag{1.10}$$

with β the porosity, R the grain radius and S_n and S_t the normal and tangential contact stiffnesses. Note that this already assumes a Hertzian contact model developed in 1882 [33] as used extensively when describing the contact between grains.

Goddard [34] notes that assumption of the Hertzian model gives $\mu \propto p^{\frac{1}{3}}$ with μ one of the elastic moduli and p the confining pressure. Using only the power law relation between $c_{p,s}$ and the moduli gives $c_{p,s} \propto \mu^{\frac{1}{2}} \propto \left(p^{\frac{1}{3}}\right)^{\frac{1}{2}} \propto p^{\frac{1}{6}}$.

Following this relation two interesting questions can be posed. If the propagation speed is indeed related to the pressure via a power law what happens in a packing with a pressure gradient? Such a pressure gradient can for instance be seen in liquids contained in a column where the pressure is proportional to the depth, $p = \rho g h$. In such a system waves propagating horizontally at greater depth would have a higher propagating speed and therefore bend upwards much like a mirage [27].

From subsection 1.1.2 we know that granular media in general form an inhomogeneous network, unlike a liquid, so that a wave propagating through the material must at least be influenced by the force chains [35]. How exactly is another question.

The second question worth asking is what happens at the top of a column of a granular medium where the confining pressure is near zero. The predicted propagation speed is then also zero. Apparently it is not possible for linear waves to propagate through this section of the medium.

Even more so, in a system without gravity it is theoretically possible to achieve a confining pressure that is very close to zero inside the whole packing, describing a packing where the particles barely touch but are not pressed together. It is these kind of systems that a large part of this report concerns itself with i.e. systems that can only be studied under micro gravity conditions.

1.2.2. Non-linear waves

Nesterenko [1] noted in 1984 that granular media can support non-linear waves. For different situations he derived non-linear wave equations [36] that were later simplified

and used by Gomez et al. [2, 3] to describe shock waves in their simulation. One such simplified equation is

$$\frac{R^2}{3}\delta_{ttxx} - \delta_{tt} + \frac{4R^2\varepsilon}{m}\left[\delta^{\alpha-1}\right]_{xx} = 0, \tag{1.11}$$

with $\delta(x,t)$ the strain field at position x and time t, R and m the radius and mass of a particle respectively and ε an interaction parameter (which depends on radii and material properties). Subscripts are partial derivatives. In the above equation α is a parameter that can change the behaviour of the equation. For $\alpha = 2$ a linear wave equation is retrieved.

Using an ansatz and minimal potential energy argument (omitted here for the sake of brevity) Gomez et al. [2] end up at Equation 1.12 which we shall use as a starting point for analysis [4]:

$$\frac{v_s}{c} = \sqrt{\frac{1}{\alpha-1}\frac{(\delta_s/\delta_0)^{\alpha-1}-2}{(\delta_s/\delta_0)-1}}, \tag{1.12}$$

with $\frac{v_s}{c}$ the ratio between non-linear wave speed and linear wave speed and $\delta_{0,s}$ the compression before and after the wavefront respectively. Clearly

$$v_s \propto \delta^{\alpha-1-1} \tag{1.13}$$

with $\delta = \frac{\delta_s}{\delta_0}$ and upon setting $\alpha = \frac{5}{2}$ to comply with the Hertzian contact potential [37]

$$v_s \propto \delta^{\frac{1}{4}}. \tag{1.14}$$

From the contact models described in Appendix E one finds a scaling law (in the case of spherical particles)

$$\delta \propto F^{\frac{2}{3}} \propto a^{\frac{2}{3}}, \tag{1.15}$$

because the acceleration a is related to the force F linearly via Newton's second law. Combining the above gives

$$v_s \propto \delta^{\frac{1}{4}} \propto a^{\frac{1}{4}*\frac{2}{3}} = a^{\frac{1}{6}}. \tag{1.16}$$

This power law has been found experimentally by van den Wildenberg [4] and is described in the mockup Figure 1.4. As seen from the picture higher confining pressures cause a bigger linear regime. It can therefore be argued that lower confining pressures will give a smaller linear regime and it is believed that at zero confining pressure no linear regime is possible (sonic vacuum) [38].

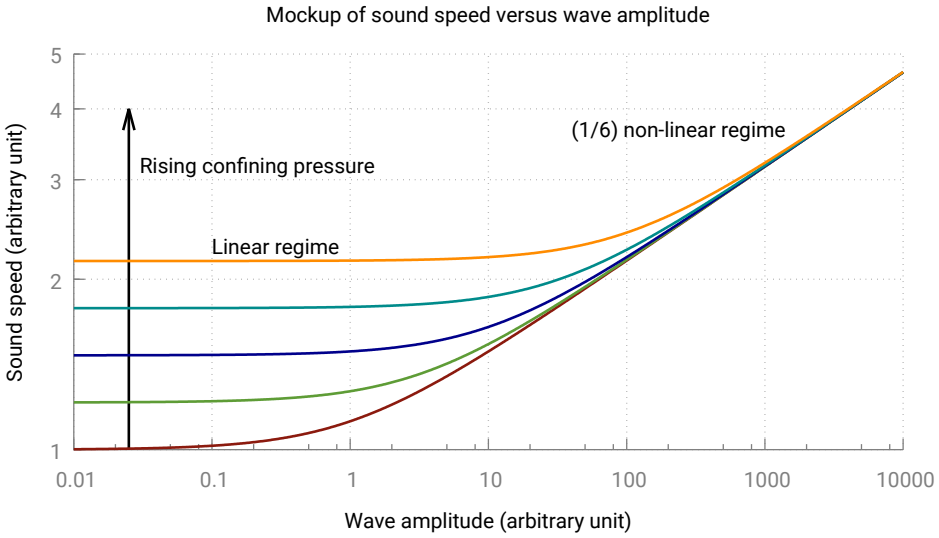

Figure 1.4.: Mockup figure with the same shape as van den Wildenberg's [4] but with arbitrary units to roughly represent the shape. The lines were drawn with shape $y = (a + x)^{\frac{1}{6}}$ with a a constant signifying confining pressure. Note that for higher confining pressures a larger linear regime (with unchanging sound speed) is witnessed. At high wave amplitudes (high x) the linear term is small and only a power-law relation remains. The transition between the two regimes moves to higher wave amplitudes with higher confining pressure.

1.2.3. Necessity

Through the phenomenon of jamming in different (non-equilibrium) microstates granular media may have different bulk properties for a single set of macroscopic parameters. The properties will depend on the interparticle contacts that can in some cases be visualised with stress-birefringent techniques such as has been done to create Figure 1.3. Other techniques include x-ray tomography, MRI and fluorescent confocal microscopy. For more info see the PhD thesis by Carpentier [39] (which lists many more techniques) and references therein or articles on specific techniques [40, 41, 42]. Although useful in some cases these techniques have some common limitations to their applicability.

It is believed that sound waves travel preferentially along force chains through the respective particle contacts [27, 35]. Depending on these contacts the properties of sound wave propagation differs. If one can describe the influence of the particle contacts on the wave it becomes possible to use a wave as a probe for the current state of the granular material. Defining the wave properties is therefore of fundamental interest.

1.2.4. Research goals

The goal of this work is to study *non-linear wave propagation in granular media* and the influence of simplified models of granular media thereon so as to provide tools for further study. To this cause three sub goals have been formulated, they are:

1. to find whether non-linear behaviour can be shown using a simple one dimensional molecular dynamics simulation with Hertzian or linear contact models.

2. to find whether a mixture of stress birefringent disks and spheres can be used as a sample in a two dimensional setup to create a simplified granular medium that still shows non-linear behaviour.

3. to increase the efficiency of an existing parabolic flight setup for time of flight measurements and prove its effectiveness with data gathered on ground and during a parabolic flight campaign.

Chapter 2.

Methods

This chapter discusses the methods used in this report. The sections describe a simulation and two different experimental setups.

"The sand doesn't care if you're made of flesh or stone"

Joaquin Lowe, 2016

2.1. Simulation

To investigate a simplified granular system a computer simulation has been made using the discrete element method (DEM) or discrete particle method (DPM) also called molecular dynamics (MD). This is a widely used method in the simulation of granular media [43]. The method has been very well described, see [44] and references therein, so only a compendious view is given here.

Given the state information ((angular) velocity, position and orientation) of all particles in a system at a certain moment and all the forces and torques on them at that moment, their movements over a finite small time interval can be approximated by several integration methods [45, 46, 47, 48, 49], among which the most notable are methods by Euler and Verlet and the Runge-Kutta and Gear-predictor methods. In essence all of these methods can be used to solve Newton's equations of motion. Integration algorithms used in this report are more thoroughly discussed in subsection 2.1.2.

After the new state of particles is calculated using one of the numerical integration methods the forces and torques on particles have to be computed again. Usually this is done by assuming a very much simplified contact model [50]. Contact models used in this report are more thoroughly discussed in subsection 2.1.3.

Software packages exist that implement the DEM; see, but do not limit yourself to, [51, 52, 53, 54, 55, 56, 57]. Each of the packages has its own unique features that define in which cases it is best applied. For the work in this thesis the author has developed yet another package so as to gain not only a large insight in the program and the ability to easily adapt it but also to gain experience from creating it.

This has resulted in a Python package tentatively called Pysim, described in subsection 2.1.1 below. The code is freely available and has a full HTML api documentation in [58].

2.1.1. Overview of Pysim DEM software

Pysim makes full use of the easy development of object oriented procedures provided by Python. It includes several classes that represent real-life entities such as particles and walls. Furthermore there is a variety of more abstract classes providing easy to imagine functionalities: a samplecell to hold all particles, an integrator to perform integration and a timeseries writer to export data to a series of files.

All these classes are replaceable by other implementations similar functionality, making Pysim very modular. This way the structure of the software can remain unchanged when changing particles from for instance a two dimensional to a three dimensional implementation.

The general flow of a typical Pysim program is depicted in Figure 2.1. In principle the blocks describe a distinct functionality that is coherent: a block does not lose it's meaning when separated from the rest of the blocks. This way blocks with similar functionality can be substituted for each other to create a program that does a different simulation. E.g. switch an Euler integrator for a Verlet integrator to gain accuracy or run the same simulation with a different set of material properties. The force calculation and integration blocks are explained in more detail below.

As the simulation of granular systems concerns itself mainly with short range forces many particles will not interact with each other instantaneously (because they are too far apart). In a system where particles do not move around a lot (jammed system) particle contacts may not even break and new particle contacts may not even be made. To avoid unnecessary computations the current implementation of Pysim assumes that once connections between particles are made during the initialization, they will not be broken and no more connections are made[1]. Depending on the force law however non-overlapping particles may still not interact with each other, so the amount of contacts is therefore only an approximation made by the user.

Since the contact between two particles may be very complicated to describe (see also Appendix E), and doing so accurately for all contacts may be time consuming, an approximation is made. First off, the particles are assumed to be perfectly spherical. This offers a wide range of contact models to be applied of which some are described in subsection 2.1.3. Note that currently only compressive models (no cohesion) and without friction (no rotation) are used[1]. For more complicated models involving these additional features please see [50].

2.1.2. Integration

Currently two integration algorithms are implemented in Pysim. The first and simplest being the Euler method, and the second being the velocity Verlet algorithm. If not mentioned otherwise the velocity Verlet algorithm is used in simulations (because of it's increased accuracy).

[1]This is the current state of implementation, however care has been taken that any extension is easily possible

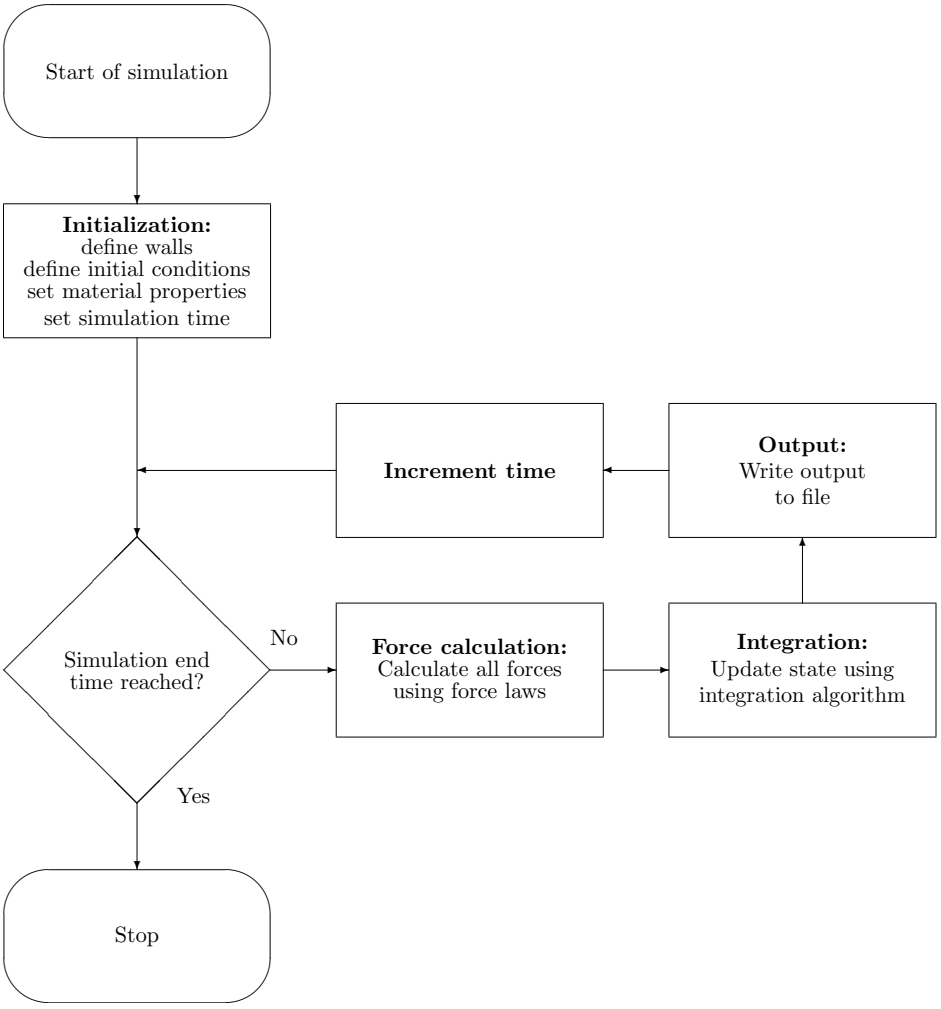

Figure 2.1.: Flowchart of a typical Pysim program. Note that all rectangular boxes can be substituted by homemade classes performing the same function, without destroying the flow of the program.

Consider Newton's equations that describe motion

$$\boldsymbol{F}_i = m_i \frac{\partial^2 \boldsymbol{r}_i}{\partial t^2}, \tag{2.1}$$

with $\boldsymbol{F}_i$ the force on particle i at position $\boldsymbol{r}_i$ and mass m_i. At any point in time the force on all particles is assumed known (since it is calculated by the contact models in another block) so that also the acceleration of all particles is known a via Newton's $\boldsymbol{a}_i = \boldsymbol{F}_i/m_i$. The same can be argued for rotational degrees of freedom but the explicit description is omitted in this report for the sake of brevity.

Euler

The Euler integration algorithm is easy to derive and implement, so it is feasible to use as an algorithm during testing. There are however disadvantages considering accuracy which is why more advanced methods are preferred, even in general.

If the position of a particle is known at a specific time, i.e. $\boldsymbol{r}_i(t_0)$, and requested at a later time, i.e. $\boldsymbol{r}_i(t_{\text{end}})$ the domain can be subdivided in (possibly equal) parts. Define the size of such a part Δt, the timestep size.

Using a Taylor expansion around the point t_0 one can find an approximation

$$\boldsymbol{r}_i(t_0 + \Delta t) = \boldsymbol{r}_i(t_0) + \Delta t \frac{\partial \boldsymbol{r}_i(t_0)}{\partial t} + \mathcal{O}(\Delta t^2). \tag{2.2}$$

The same argument can be made for the velocity, so that a single timestep, that can be repeated over and over, forms

$$\boldsymbol{r}_i^{n+1} = \boldsymbol{r}_i^n + \boldsymbol{v}_i^n \Delta t \tag{2.3}$$

$$\boldsymbol{v}_i^{n+1} = \boldsymbol{v}_i^n + \frac{\boldsymbol{F}_i^n}{m_i} \Delta t, \tag{2.4}$$

where the superscripts n and $n+1$ denote information at the current timestep (with known information) and the information at the next (unknown) timestep respectively.

Note that the $\mathcal{O}(\Delta t^2)$ have been omitted, making a single timestep second order accurate in timestep size. Because the whole domain has to be divided in $\mathcal{O}(\frac{1}{\Delta t})$ timesteps, the total accuracy of the Euler integration algorithm is said to be of the first order in Δt.

Velocity Verlet

To derive the velocity Verlet algorithm split the second order differential equation of motion into two first order differential equations

$$\frac{\partial \boldsymbol{r}_i(t)}{\partial t} = \boldsymbol{v}_i(t) \qquad\qquad \frac{\partial \boldsymbol{v}_i(t)}{\partial t} = \frac{\boldsymbol{F}_i(t)}{m_i}. \tag{2.5}$$

An expansion of both quantities around $t + \Delta t$ gives

$$\boldsymbol{r}_i(t + \Delta t) = \boldsymbol{r}_i(t) + \Delta t \boldsymbol{v}_i(t) + \frac{\Delta t^2}{2m_i} \boldsymbol{F}_i(t) + \mathcal{O}(\Delta t^3) \tag{2.6}$$

$$\boldsymbol{v}_i(t + \Delta t) = \boldsymbol{v}_i(t) + \Delta t \frac{\partial \boldsymbol{v}_i(t)}{\partial t} + \frac{\Delta t^2}{2} \frac{\partial^2 \boldsymbol{v}_i(t)}{\partial t^2} + \mathcal{O}(\Delta t^3). \tag{2.7}$$

Using another Taylor expansion to find that

$$\frac{\Delta t^2}{2} \frac{\partial^2 \boldsymbol{v}_i(t)}{\partial t^2} = \frac{\Delta t}{2} \left(\frac{\partial \boldsymbol{v}_i(t + \Delta t)}{\partial t} - \frac{\partial \boldsymbol{v}_i(t)}{\partial t} \right) + \mathcal{O}(\Delta t^3) \tag{2.8}$$

it can be found that

$$\boldsymbol{v}_i(t+\Delta t) = \boldsymbol{v}_i(t) + \frac{\Delta t}{2m_i}\left(\boldsymbol{F}_i(t+\Delta t) + \boldsymbol{F}_i(t)\right) + \mathcal{O}(\Delta t^3). \tag{2.9}$$

The above can be formed into a repeatable procedure, with superscripts as above,

$$\boldsymbol{r}_i^{n+1} = \boldsymbol{r}_i^n + \Delta t \boldsymbol{v}_i^n + \frac{\Delta t^2}{2m_i}\boldsymbol{F}_i^n \tag{2.10}$$

$$\boldsymbol{v}_i^{n+1} = \boldsymbol{v}_i^n + \frac{\Delta t}{2m_i}\left(\boldsymbol{F}_i^n + \boldsymbol{F}_i^{n+1}\right). \tag{2.11}$$

2.1.3. Contact models

To approximate the interaction force between two (assumed before) spherical particles i and j the force is assumed to be only related to their overlap δ_{ij}. In general the overlap depends on the particle positions $\boldsymbol{r}_{i,j}$ and their radii $R_{i,j}$ as

$$\delta_{ij} = (R_i + R_j) - \|\boldsymbol{r}_i - \boldsymbol{r}_j\|. \tag{2.12}$$

This is also depicted in Figure 2.2 in a one dimensional case for simplicity. The definition is however vectorially defined in higher dimensions.

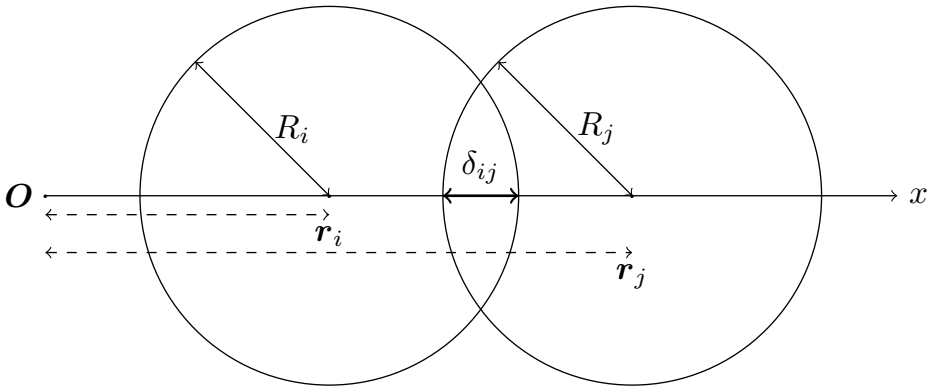

Figure 2.2.: Two particles in contact in a 1D system. The overlap δ_{ij} depends on the particles positions $\boldsymbol{r}_{i,j}$ and their radii $R_{i,j}$.

The contact models used in the simulations are described below. For clarity the subscripts denoting particles are omitted.

Linear compressive particle and a wall

This section describes how a linear compressive particle interacts with a wall. The model is linear because $\boldsymbol{F}(\delta) \propto \delta$ and compressive because $\boldsymbol{F} = 0$ when $\delta <= 0$

$$\boldsymbol{F}(\delta) = \begin{cases} -k\delta \cdot \boldsymbol{n}, & \text{for } \delta > 0 \\ \boldsymbol{0}, & \text{otherwise} \end{cases}. \tag{2.13}$$

Additionally $\boldsymbol{F}(\delta) = \boldsymbol{0}$ when the particle is on the outside of the wall. This can be calculated using the equations in Appendix D.

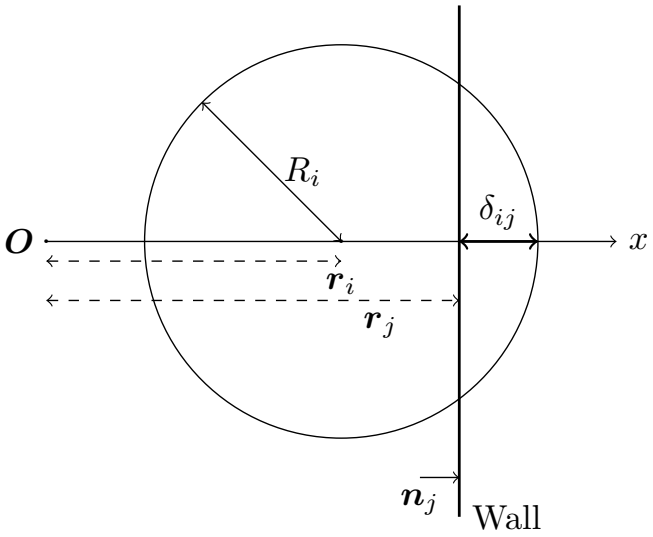

Figure 2.3.: A particle at position $\boldsymbol{r}_i$ and radius R_i in contact with a wall at position $\boldsymbol{r}_j$ and outward pointing normal $\boldsymbol{n}_j$ so that the overlap is δ.

Two linear compressive particles

This section describes the contact law between two particles if they only exert compressive forces on each other via a linear law.

Each particle follows the equation of the linear oscillator $F = -k\delta$ with $|F|$ the magnitude of exerted force at excitation δ and k the spring constant. Equating the forces for particle i and j gives a relation for the magnitude of the mutual force, that must be equal for both particles.

$$F_i = F_j. \tag{2.14}$$

Inserting a linear relation between the overlap δ and the force for both particles (with k a constant for stiffness)

$$\delta_i k_i = \delta_j k_j. \tag{2.15}$$

Then define $\delta = \delta_i + \delta_j$ to find

$$(\delta - \delta_j)k_i = \delta_j k_j, \tag{2.16}$$

$$\delta_i = \delta\frac{k_j}{k_i + k_j} \qquad \delta_j = \delta\frac{k_i}{k_i + k_j} \tag{2.17}$$

$$F = \delta\frac{k_i k_j}{k_i + k_j}. \tag{2.18}$$

The final relation for the force on particle i by particle j then becomes

$$\boldsymbol{F}_{i,j}(\delta) = \begin{Bmatrix} -F\boldsymbol{n}_{ij}, & \text{for } \delta > 0 \\ \boldsymbol{0}, & \text{otherwise} \end{Bmatrix}. \tag{2.19}$$

Two Hertzian spheres

The contact between two Hertzian spheres is described, see Appendix E, as

$$\delta = \left(\frac{9}{16RE^{*2}}\right) F_H^{\frac{2}{3}} \tag{2.20}$$

which can be rearranged to find

$$F_H = \delta^{\frac{3}{2}} \left(\frac{9}{16RE^{*2}}\right)^{-\frac{1}{2}} \tag{2.21}$$

(Note that Appendix E uses the symbol P to comply with literature, we will here use F_H). Note that R is here the effective radius satisfying $1/R = 1/R_i + 1/R_j$ and E^* the effective modulus satisfying $1/E^* = (1-\nu_i^2)/E_i + (1-\nu_j^2)/E_j$.

Following the same reasoning as before the force on particle i is found by using the normal

$$\boldsymbol{F}_{i,j}(\delta) = \begin{Bmatrix} -F_H \boldsymbol{n}_{ij}, & \text{for } \delta > 0 \\ \boldsymbol{0}, & \text{otherwise} \end{Bmatrix}. \tag{2.22}$$

Hertzian sphere and a wall

The case for compression of two spheres can be simplified in the case that a single sphere is in contact with a wall, by making the second sphere of infinite radius and infinite modulus so that

$$1/R = 1/R_i \qquad\qquad 1/E^* = (1-\nu_i^2)/E_i. \tag{2.23}$$

Otherwise the model remains unchanged.

Two Hertzian cylinders

From Appendix E see that

$$\delta = \frac{4}{\pi E^* L} \cdot F \tag{2.24}$$

so that

$$F = \delta \frac{\pi E^* L}{4}, \tag{2.25}$$

using $1/R = 1/R_i + 1/R_j$ and $1/E^* = (1-\nu_i^2)/E_i + (1-\nu_j^2)$. L is the length of a cylinder. Note that it is assumed that the cylinders are of the same length. In other cases a different model can be used, see [33, 59, 60].

Following the same reasoning as before the force on particle i is found by using the normal

$$\boldsymbol{F}_{i,j}(\delta) = \begin{Bmatrix} -F \boldsymbol{n}_{ij}, & \text{for } \delta > 0 \\ \boldsymbol{0}, & \text{otherwise} \end{Bmatrix}. \tag{2.26}$$

Hertzian cylinder and a wall

This case differs only from the two Hertzian cylinders contact for R and E^* which satisfy in this case

$$1/R = 1/R_i \qquad\qquad 1/E^* = (1-\nu_i^2)/E_i. \tag{2.27}$$

Hertzian sphere and Hertzian cylinder

From Appendix E one can approximate the contact between a cylinder and a sphere with

$$\delta = \kappa\,(2Q)^{\frac{2}{3}} \left(\frac{1}{R_1\left(-\frac{1}{e}\frac{\mathrm{d}\mathcal{E}}{\mathrm{d}e}\right)} \right)^{\frac{1}{3}} \cdot F^{\frac{2}{3}}. \tag{2.28}$$

Note here that κ and $-\frac{1}{e}\frac{\mathrm{d}\mathcal{E}}{\mathrm{d}e}$ are related to full elliptical integral solutions of which Puttock gives numerical approximations [61] and $Q = \frac{3}{4}\left(\frac{1-{\nu_1}^2}{\pi E_1} + \frac{1-{\nu_2}^2}{\pi E_2}\right)$.

After rearrangement one finds

$$F = \frac{\delta^{\frac{3}{2}}\kappa^{-\frac{3}{2}}}{2Q} \left(\frac{1}{R_i\left(-\frac{1}{e}\frac{\mathrm{d}\mathcal{E}}{\mathrm{d}e}\right)} \right)^{-\frac{1}{2}}. \tag{2.29}$$

2.2. On-ground experiments

To perform experiments on ground a sample cell was constructed capable of holding a layer of particles. The system therefore is essentially two dimensional, whereas the particles in it are three dimensional (spheres and/or cylinders). The sample cell is shown in Figure 2.5 and part of a larger setup that includes a Phantom V711 high speed camera and a shaker (LDS air cooled vibrator v721) with its appropriate driving soft- and hardware as distributed by the manufacturer. The complete setup is shown in Figure 2.4.

2.2.1. Setup overview

Light emitted by a light source (either daylight or a lamp or both) travels through a circular polarizer (constructed out of a linear polarizer and a quarter wave plate) placed between the sample cell and the light source. The circular polarizer (not visible in the pictures) is placed very closely to the sample cell so (almost) no other light can enter the sample cell.

To avoid unwanted fringes in the resulting image stress free perspex sheets have been used as a containing material, along with aluminium for the load bearing parts. The perspex has been freed of load by giving it a few fractions of a millimetre of play in all directions. This way only phase changes caused by the sample will show up in the resulting image.

The camera is outfitted with a lens of 50 [mm] focal length and aperture $\varnothing = 52$ [mm] and a $\varnothing = 58$ [mm] circular polarizer in the opposite polarization direction of the first one effectively creating a circular polariscope.

The polariscope maps the stress intensity of a stress birefringent material to intensity of the light it lets pass. For a more detailed view of the polariscope and more information on polarization in general please refer to Appendix C.

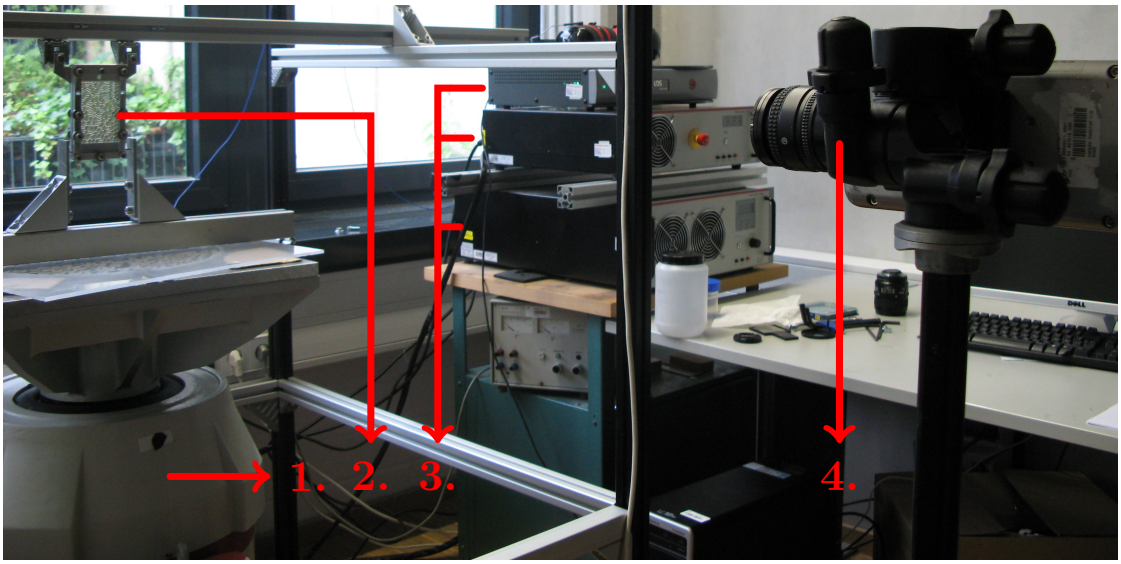

Figure 2.4.: The complete setup for on ground experiments. Visible are *1.* The shaker *2.* The sample cell *3.* Shaker control unit, power supply and power amplifier *4.* High speed camera.

2.2.2. The sample cell

To reduce friction between the cell walls and the sample the cell has been made slightly larger (3.1 [mm]) than the intended sample diameter (3 [mm]). This extra space allows the sample to move more freely but keeps the contacts between particles roughly in plane. It is likely that friction between the cell and sample was hereby reduced but not completely removed. The magnitude and effect of this friction have not been studied thoroughly.

Instead we note that the frictional force between a particle and the wall is smaller than the gravitational force on a particle, because the particles fall out of the sample cell when hold upside down. The weight of the particles (ca. 13 [g]) is much smaller than the weight of the top of the container (29.2 [g]) and the mass of the weight that is dropped (44.0 [g]).

Frictional forces with the walls increase when the packing is compressed to the point where particles no longer drop out of the cell. The packing is therefore relaxed (by tapping) before every experiment until no strong force chains are visible.

Furthermore the driver and top plate for pressure application have been designed slightly shorter than the sample cell width so as to allow frictionless (as far as possible) motion between them.

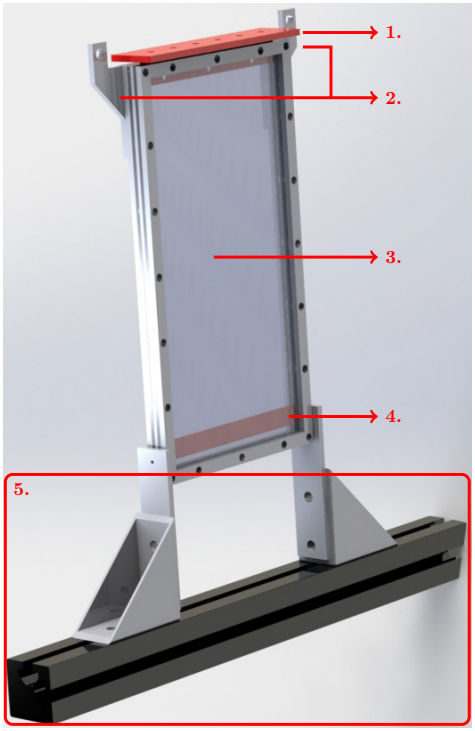

(a) CAD rendering of the sample cell, visible are *1.* Moveable top plate to provide pressure using weights *2.* Connector plates to connect the sample cell to the non moving reference frame *3.* Stress free perspex sheets *4.* Moveable driver *5.* Parts used for connecting the driver to the shaker.

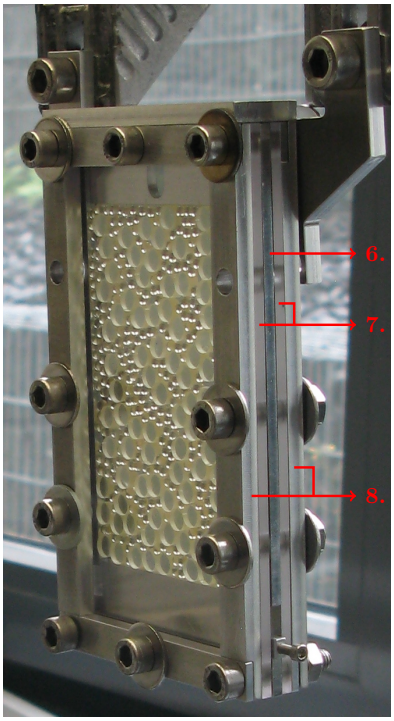

(b) Picture of the sample cell in the setup, with the driver detached from the shaker for clarity of the picture. Visible are *6.* Side wall in contact with the particles *7.* Stress free perspex sheets *8.* Reinforcements.

Figure 2.5.: Two dimensional sample cell for stress birefringent experiments on ground.

2.2.3. Particles

Two types of particles were used for the experiment both consisting of stress birefringent material produced by Vishay [62]. The first type are disks in varying diameter cut with a waterjet from 3 [mm] thick sheet with tradename PS-4.

The second type of particle are spheres that were hand made from PL-3 using the procedures outlined in [63, 64]. The process mainly involves mixing the two raw components for PL-3 (a resin and a hardener, the exact composition of which are kept trade secret by the manufacturer) and using a pipette to create droplets of the desired size.

The droplets are then dropped in a large cylinder filled with a liquid of similar but lower density as the resin-hardener mixture so that the droplets fall slowly through the liquid. Care is taken that the liquid and the resin-hardener mixture do not naturally mix so that surface tension causes the droplets to become spherical. In our case the liquid was silicon oil produced by the Silicon Profis under tradename Elbesil Öl AK 60.000 or Elbesil Öl B 60.000 (which differ only in tradename, 60.000 is the kinematic viscosity in $\times 10^{-6}$ $\left[\mathrm{m}^2/\mathrm{s}\right]$) [65]. The droplets harden into PL-3 particles on their way down through the oil. A picture of the cylinder with particles dropped in can be seen in Figure 2.6.

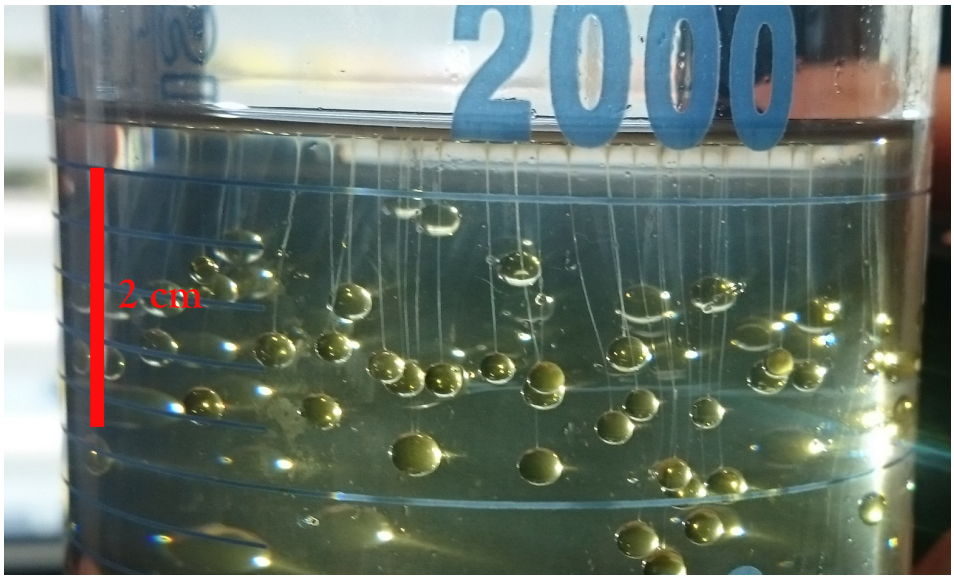

Figure 2.6.: Droplets in a cylinder of silicon oil during the hardening process into particles. Note that some particles drop faster than others according to their size [64], but the average drop speed is in the order of several centimeters per hour. The particles leave traces of slimy-looking waste that contaminates the silicon oil. For repeated production the silicon oil therefore has to be replaced (or cleaned).

The particles were then mechanically cleaned by hand using absorbing paper sheets and their diameter was evaluated with the use of a caliber. Although the exact required volume of a sphere can be calculated using $V = 4/3\pi R^3$, the particles still differ in size mainly due to the inaccuracy of the pipette. Roughly 70% of the particles produced were in the desired range ($2.9 \leq \varnothing \leq 3$ [mm]). Particles outside this size range are left unused.

Material	Strain optical coeff. K	Elongation [%]	Young's modulus E [GPa]	Poisson's ratio ν
PS-4	0.009	> 40	0.004	0.500
PL-3	0.002	> 50	0.0014	0.42

Table 2.1.: Material properties of two materials distributed by Vishay.

2.3. Zero gravity experiments

To achieve a full 3D sample a granular medium near the jamming transition the sample is taken aboard the Airbus A310 ZERO-G aircraft for parabolic flights. Below the setup and procedures are explained.

2.3.1. Experimental setup

Hardware

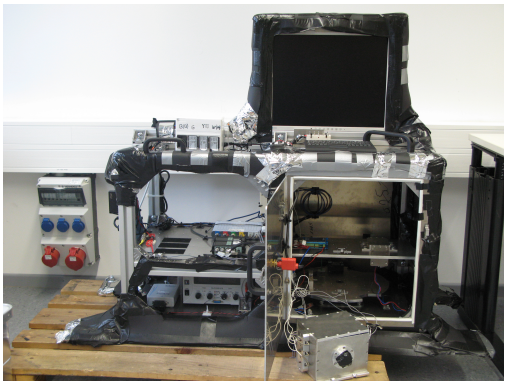

(a) The rack with the door open and sample cell taken out for clarity of the picture.

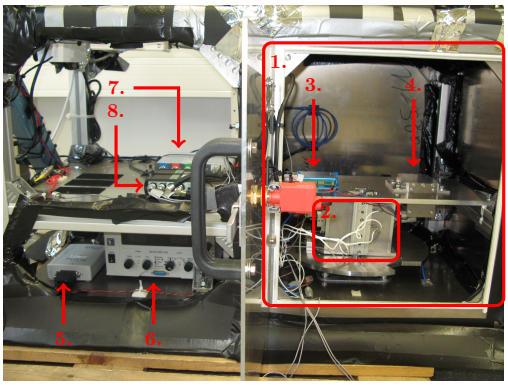

(b) Overview of devices in the rack with *1.* Outside of double container *2.* Sample cell *3.* Motor driver *4.* Motor *5.* PicoLog data logger *6.* DC power supply *7.* PicoScope digital oscilloscope *8.* Sensor pre-amplifiers. Additional sensor amplifiers are not shown.

Figure 2.7.: Parabolic flight rack.

The rack used in the parabolic flight campaign is shown in Figure 2.7. The rack was bolted to the floor of the airplane so that it was unable to move. A mini PC (not visible in picture) was used to control the data acquisition modules. Most noticeable is the double containment for the sample, so that beads can under no circumstances exit the setup. Furthermore the sample cell is placed on a damper to overcome vibrations from the plane and experimenters. The flight procedure is further explained in subsection 2.3.2.

Sensors (see below) are connected through the throughputs in the sample cell (see

below) to sensor amplifiers. The sensors were then connected to data logging modules. The piezo sensor and accelerometers are connected to a PicoScope 5000a series digital oscilloscope sampling at 1 [MHz] a voltage range in 14 [bit]. The voltage range differs from ±10 [V] (maximum output of sensors and amplifiers) to ±100 [mV] depending on the signal strength. In general the largest range was used (since accuracy was not an issue) unless this introduced too much noise for the automatic analysis software (see below) to function properly. The pressure sensors were connected to a PicoLog 1000 series sampling at 12 [bit] a voltage range of 0 to 5 [V] at 10 [Hz].

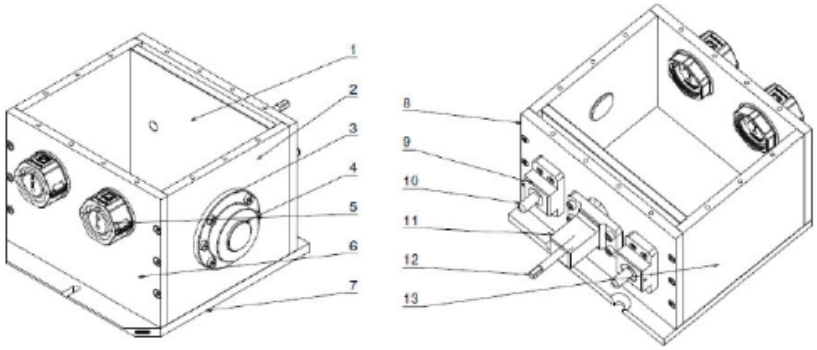

(a) CAD drawing (line rendered) of the sample cell. Shown are: *1.* moveable (mobile) wall *2.* side wall #1 *3.* plunger fixation adapter *4.* plunger *5.* feed through (for wires) *6.* front wall *7.* bottom (wall) *8.* back wall *9.* linear guide for mobile wall *10.* linear guide for mobile wall *11.* external pressure (P_0) control screw housing *12.* external pressure control shaft *13.* side wall #2

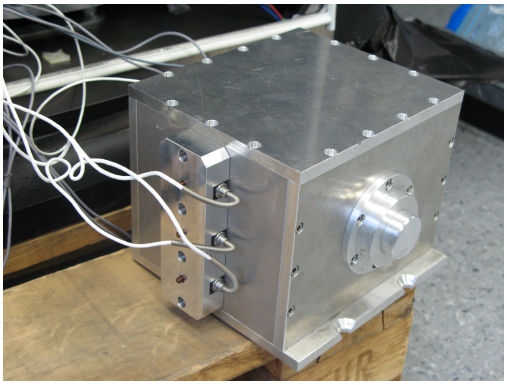

(b) The sample cell. On the right one can see the plunger (also in Figure 2.8c) that the hammer will hit. Furthermore three wires are visible that are connected to three pressure sensors.

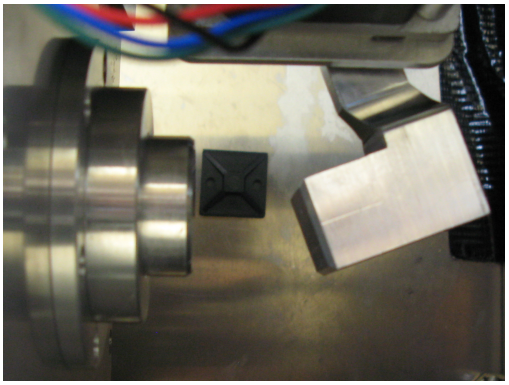

(c) The plunger (left) and hammer (right).

Figure 2.8.: The sample cell with hammer.

The hammer was driven using a stepper motor and motor driver (SMCI33-2). The motor driver was capable of remembering several movement profiles that were set using

the mini PC pre-flight. Using a digital signal from the PicoLog the motor was triggered to run a profile. The profile to run was selected by using several three point switches, located near the keyboard for ease of access, acting as a binary counter (0 to 31).

The sensors, visible in Figure 2.9, were placed around the center of the packing at a distance from each other. The distance was measured using a ruler at the same distance from the camera as the sensors.

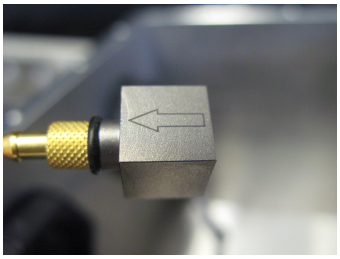

(a) Close-up of the accelerometer (Miniature DeltaTron 4508B series).

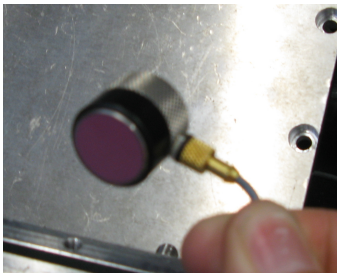

(b) Close-up of the piezo sensor.

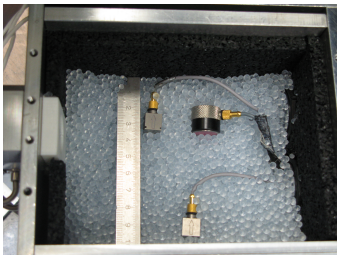

(c) Sensors placed in sample.

Figure 2.9.: Placement of the sensors in the sample cells. The ruler is only used to measure the distance between the sensors, and the sensors are placed so that they do not lie directly in the path of the wave and could shield each other.

Sample

The sample, or packing, consists of the sample cell filled with glass beads (so spherical of shape) of 3 and 4 [mm] diameter (to avoid crystallization) at a ratio so that their volume is approximately equal. The particles were poured in from a plastic container almost until the brim. The last particles were inserted by using a spoon. Afterwards the packing was relaxed by tapping (and adding more particles if necessary) and by cyclic compression by hand. Around 20 load cycles were performed to relax the packing, inspired by [66, 67]. Not relaxing the packing causes very inconsistent results among the first experiments as the packing is then in the process of relaxing.

2.3.2. Flight procedure

A single parabolic flight campaign (PFC) consisted out of 3 flight days. Every day had one flight lasting approximately 3.5 [h]. The largest portion of this time is used for take-off and landing and for flying to an otherwise much unused stretch of sky above the ocean. During the flight there are 31 flight procedures resembling a parabolic shape, for the sake of ease called parabolas from here on. The parabolas are divided in groups of 5, except for the first group (6). After every group there is a break of either 5 or 8 minutes of steady flight. A parabola itself lasts around 1 [min] but is appended with a period of steady flight so that a parabola is only repeated every 3 [min]. A single parabola is shown in Figure 2.10.

During a parabola two different recordings of data were made. One in the microgravity phase and one in the hypergravity phase after the parabola. In some cases additional steady flight data was also logged. This way the influence of gravity could be directly measured since the packing will, as assumed, change little in this short period of time. The pilots callouts listed in Figure 2.10 were used as a countdown so the experimenters know when to start or stop a measurement.

2.3.3. Data acquisition

Two hardware devices were used to acquire data. First the PicoScope 5000a digital oscilloscope for the accelerometer and piezoelectric data. It was set at a sampling frequency of 1 [MHz]. Furthermore a PicoLog 1000 was used at a frequency of 10 [Hz] to capture pressure data. Both were connected to the mini PC using a high speed USB connection. The manufacturer supplied drivers were used to create a custom user interface to the devices.

The custom built interface allowed to choose several settings for the oscilloscope. Most importantly it was set to trigger on channel A (the channel for the first accelerometer). Whenever the voltage surpassed a trigger value a sample was collected and a data file created. The file contains 25000 samples, 5000 samples before and 20000 after the trigger sample. The controlling software was written specifically for this purpose, however, is too complicated to be explained here. Instead, a screenshot of it is provided in Figure 2.11 and the code is available including user documentation and API documentation upon request at the author.

Every datafile is stored on hard drive. To quickly show the experimenter what is happening an automatic analysis tool has been written. It uses a peak detection algorithm to make an estimate for the time of flight (the time it takes for the wave to travel from the first to the second sensor). The experimenters were able to set the distance between the sensors so that an estimate for the propagation speed was possible. This was plotted on the vertical axis with the geometric mean of the peak heights on the horizontal axis.

To avoid overloading the processor with this rather extensive procedure it was made possible to process only every N^{th} file. The code is available upon request with the author including user documentation and API documentation.

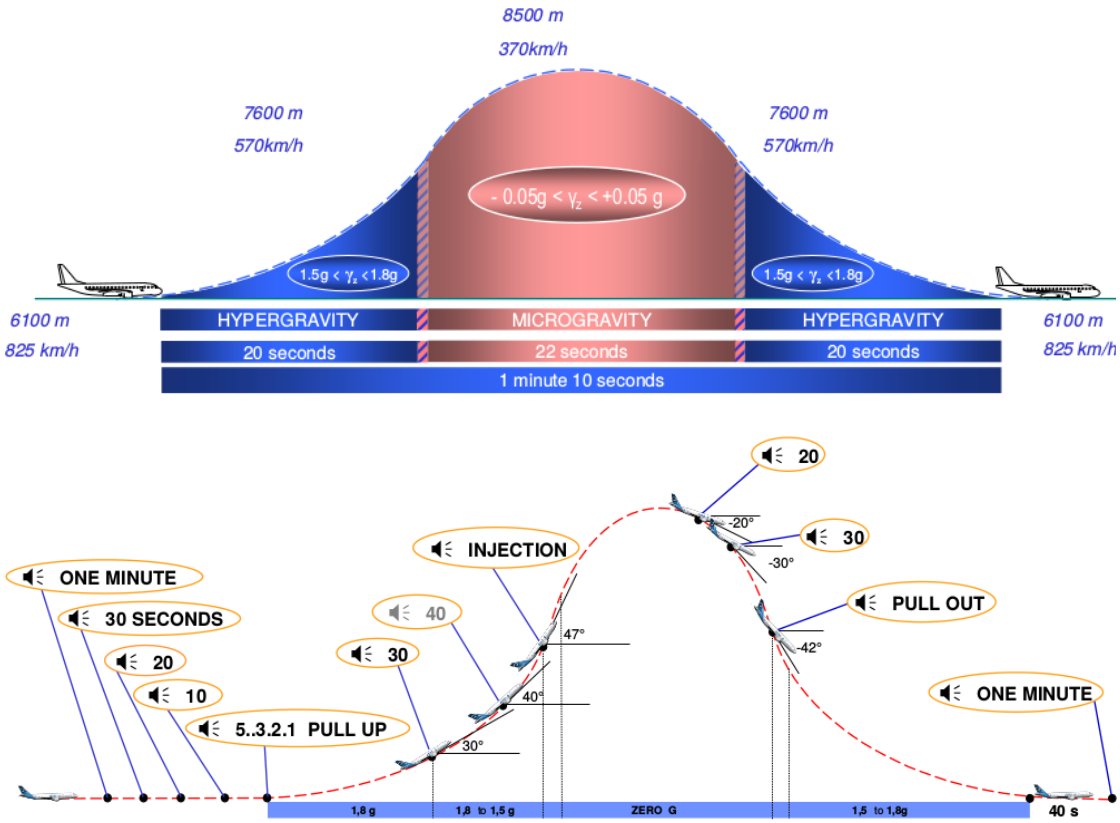

Figure 2.10.: Schematics showing a single parabola. Images from Novespace safety instructions [68]. *top:* Schematic view of time passed during a single parabola. Note that hypergravity phases are separated from the microgravity phase by a transition period in which the magnitude of gravity quickly changes. Furthermore the aircraft velocity and altitude are given at key points during the procedure to show how aggressive the procedure is. *bottom:* Schematic view of the flight path during a single parabola where the pilot's callouts are given. The callouts are given at key points during the procedure and can therefore be used as a countdown to the three different phases.

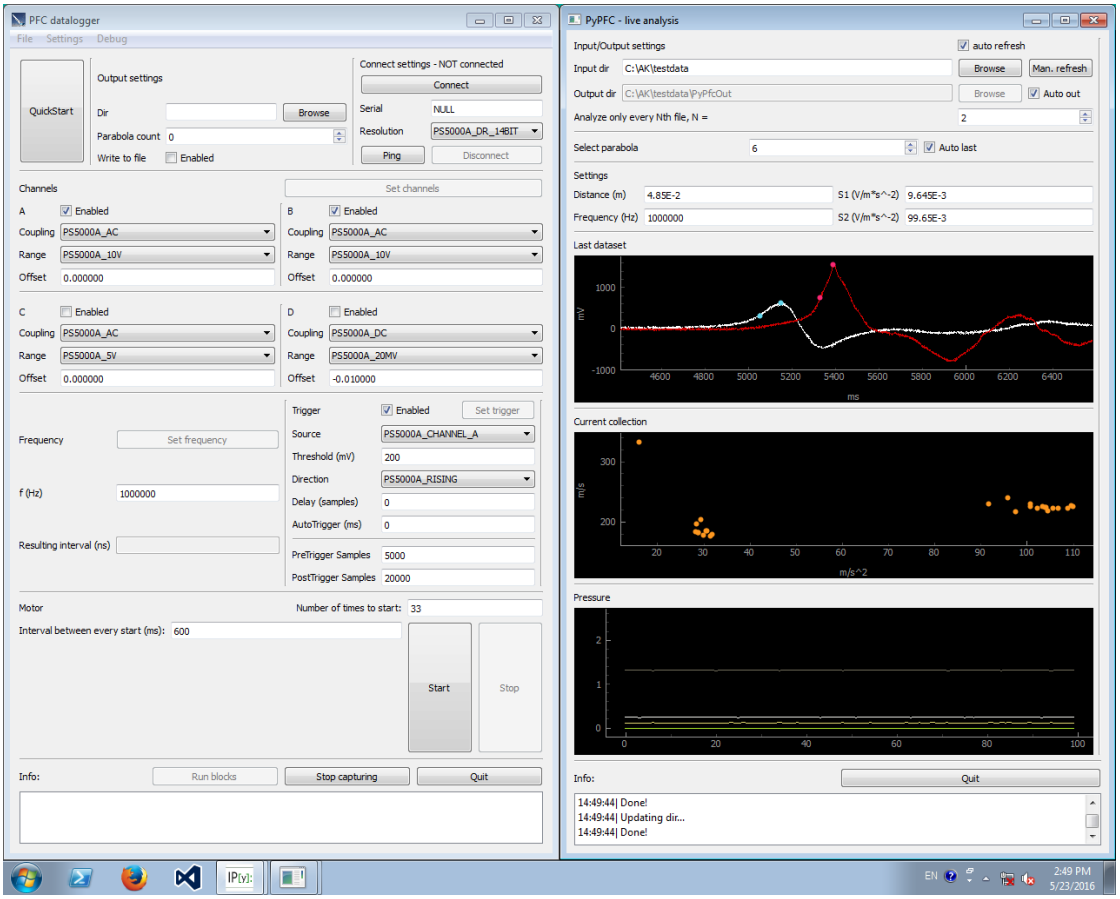

Figure 2.11.: Screenshot of the controlling software during the parabolic flight. *left:* The interface to the capture devices, allowing to set all acquisition parameters during operation. This part also provided the experimenters with feedback on whether sound signals were captured. *right:* The automatic analysis interface that shows one of the last datafiles gathered (top). Furthermore using the automatic analysis tool the current dataset (parabola) is plotted in the middle figure. The bottom figure contains the last 10 [s] of pressure data for all pressure sensors. The green line shows the external pressure and the other three lines show the pressure at different heights in the packing.

Chapter 3.

Results

This chapter discusses experimental results and results from simulations conducted using the methods outlined in chapter 2.

"To see a world in a grain of sand"
William Blake, 1789

3.1. Simulation

This one dimensional simulation was conducted using the Pysim package described above (in section 2.1). As a model system a chain of particles is chosen, the first timestep of which can be seen in Figure 3.1. The particles have a radius of 3.0 [mm]. A system of 100 particles is considered, with the particles separated by a distance d. This distance may vary per particle pair and may very well be negative (simulating a compressed chain). With an interparticle distance of $d = 0.001$ [mm] part of the simulation can be seen in an animation[1]. The initial velocity was 10 [m/s] and timestep size 1×10^{-5} [s].

3.1.1. Linear contact model

A typical velocity profile is shown in Figure 3.2. The distance between the peaks, in relation to the the distance between the particles, gives an expression for the propagation speed of the wave. Note that this is not the only way to determine the propagation speed. Different methods (not used here) exist that may lead to (slightly) different results. For a disambiguation see [69].

The arrival times of the wave at each particle, defined as the first timestep a particle starts moving in the positive x-direction, are plotted in Figure 3.3. The slope of the lines increase for larger inter particle distance d meaning a longer time of flight between particles. For $d < 0$ all lines collapse showing a system that is qualitatively different from the case where $d > 0$. This is reflected from the different velocity profiles shown in this case, depicted in Figure 3.4.

For cases where $d > 0$ a simple model can be made to predict the propagation speed of the wave (S. Luding, personal communication):

$$c = \frac{d + 2R}{t_c + \frac{d}{v_0}}, \tag{3.1}$$

[1] https://kamphuisalex.stackstorage.com/index.php/s/ncynh7k940H5cDd

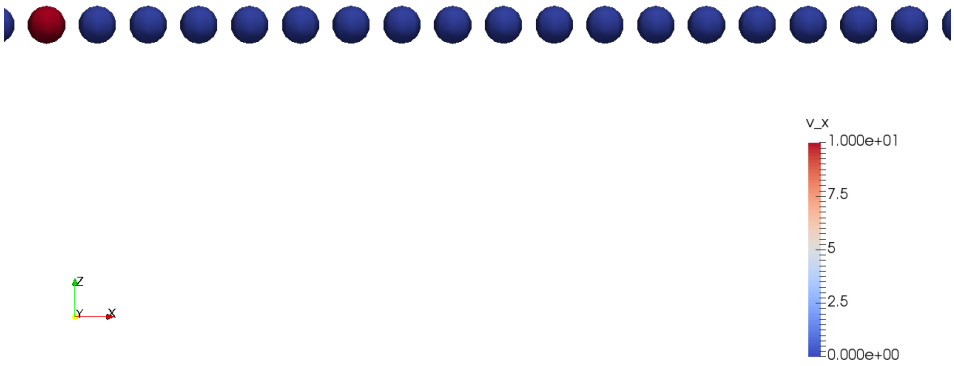

Figure 3.1.: Simulation of a chain of particles. The particles have equal radii and they are separated by a distance d. The red particle is given an initial velocity to the right (positive x direction). The blue particles have an initial velocity identical to 0.

with v_0 the initial speed of the excited particle. The expression can be thought of as follows; the propagation speed is the distance travelled per particle (so the distance from a particle to the next and the diameter of that particle together) divided by the time it takes to travel. This time is the sum of the contact time t_c and the time it takes to travel a distance d.

Following Luding [50] the contact time

$$t_c = \frac{\pi}{\omega}, \tag{3.2}$$

with $\omega = \sqrt{2k/m}$ (with m the mass and k the stiffness). We used the parameters in Table 3.1 and the contact model in Appendix E for a cylinder-cylinder contact (which is linear) to find that

$$k = \frac{\pi E^* L}{4} \approx 1963.5 \text{ [N/m]} \tag{3.3}$$

$$t_c = 4.77 \times 10^{-4} \text{ [s]}\,. \tag{3.4}$$

Using this contact time in Equation 3.1 gives the theoretical fit in Figure 3.5. The optimized fit gives a contact time of $t_{c,\text{fit}} = 2.37 \times 10^{-4}$ [s].

3.1.2. Hertzian contact model

For an inter particle separation $d > 0$ the chain of Hertzian spheres (Figure 3.6) does not behave qualitatively different from the chain of cylinders (Figure 3.5). For $d < 0$

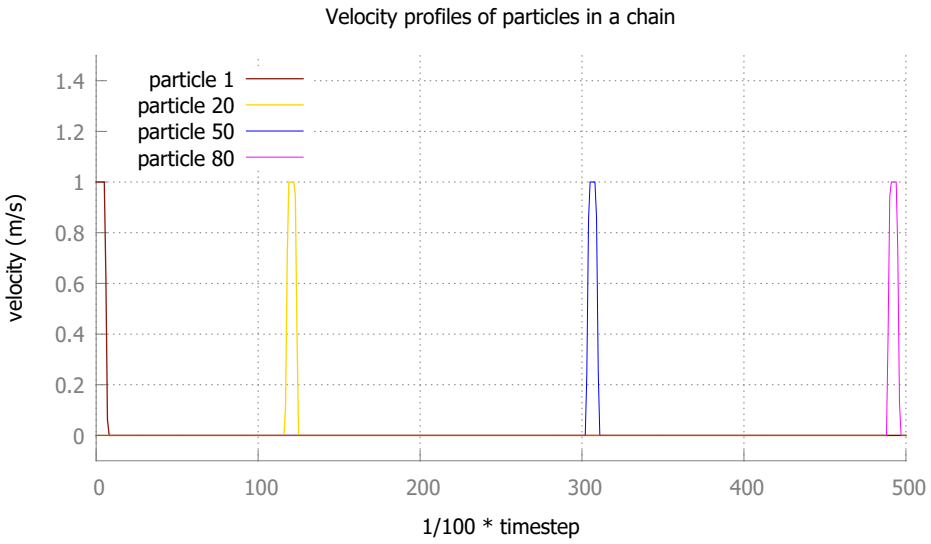

Figure 3.2.: Velocity profiles of several selected particles in a chain of particles, interacting via a linear contact model. Note that every particle reacts the same way to the disturbance (wave), just on a later time. The inter particle distance d is 0.001 [m].

however, the chain with spheres shows an increase in sound speed initially. This may be attributed to the fact that under compression the sphere becomes stiffer (due to the non-linearity in the contact law). The sound speed naturally moves faster through stiffer particles.

When d decreases even more (in this case $d < -0.0002$ [m]) the sound speed starts dropping again. This may be attributed, similar as in the Hertzian cylinder (linear) case, to the reduced distance between particles. Reducing this distance means that between two points in space there are more particle contacts (each slowing down the wave via t_c).

The animation of this wave (not shown) tells us that the first excited particle is unable to transfer all of its kinetic energy to the second particle (see also the velocity profile in Figure 3.4). Instead it is partly reflected backwards. This leaves the propagating wave front with less energy. Although not conclusively, this suggests that the amount of energy in the wave may influence the propagation speed as suggested by Gomez [2, 3] and shown experimentally by a group in Leiden [4].

3.1.3. Varying initial velocity

Another set of simulations was run using the parameters in Table 3.2, now varying the initial velocity of the excited particle. The initial velocity is a measure for the wave amplitude, and so one expects a faster wave following subsection 1.2.2. Note that the timestep size used is 100 times smaller ($\frac{1}{5} \times 10^{-7}$) to account for the faster moving particles. It is possible to increase the initial velocity even more, but this requires an even

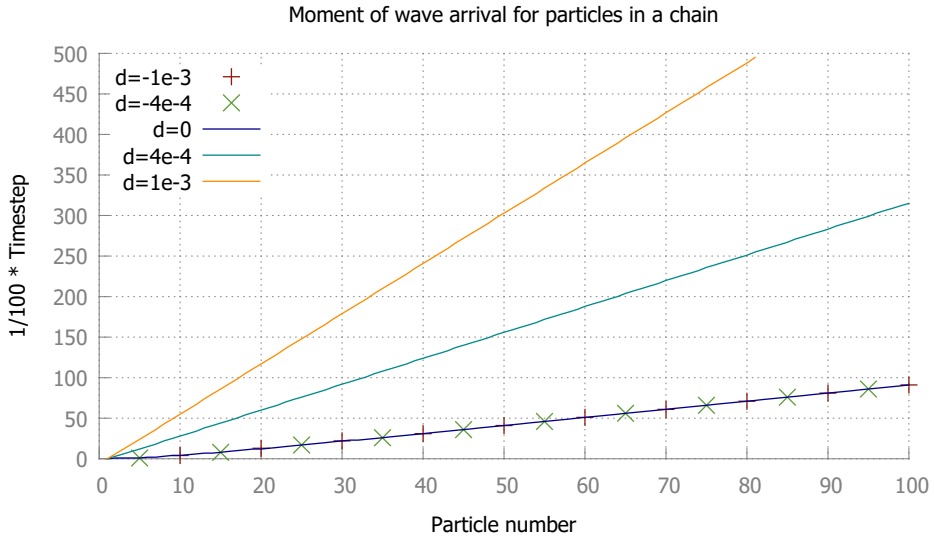

Figure 3.3.: Wave arrival times for different inter particle separations. Note that the slope increases for increasing inter particle separation d. This means the wave takes longer to get to the next particle when the distance is longer. Furthermore the lines for $d < 0$ collapse (with the line for $d = 0$) and have therefore been plotted with crosses on only a few data points.

smaller timestep size and simulation of a reasonable system size becomes impractical. The maximum initial velocity used here (10 [m/s]) should be more than enough to show the behaviour from section 3.2.

The relation between initial velocity and wave propagation speed can be seen in Figure 3.7. For the two particle types (Hertzian spheres and Hertzian cylinders (linear)) the propagation speed increases with initial velocity. Note that the curves are (almost everywhere) straight in the log-log plot. A powerlaw can therefore be fit. The yellow line (linear contact) has a slope of 2.04×10^{-2} and the red linear similarly so. The relation is therefore clearly not linear, nor constant or equal to the $\frac{1}{6}$ power-law expected from subsection 1.2.2.

A stronger increase in propagation speed can be seen at the last data point (where initial velocity $v_0 = 10$ [m/s]). Even this increased slope is not sufficient to come close to the $\frac{1}{6}$ power-law. Furthermore the point looks ill-placed in relation to the others, which hints towards a numerical error. A possible numerical error made in this case is a too large timestep size for the high particle velocity. This could be confirmed by further decreasing the timestep size in another simulation but as this is impractical for multiple simulation and the conclusion would remain unchanged, a rerun is omitted here.

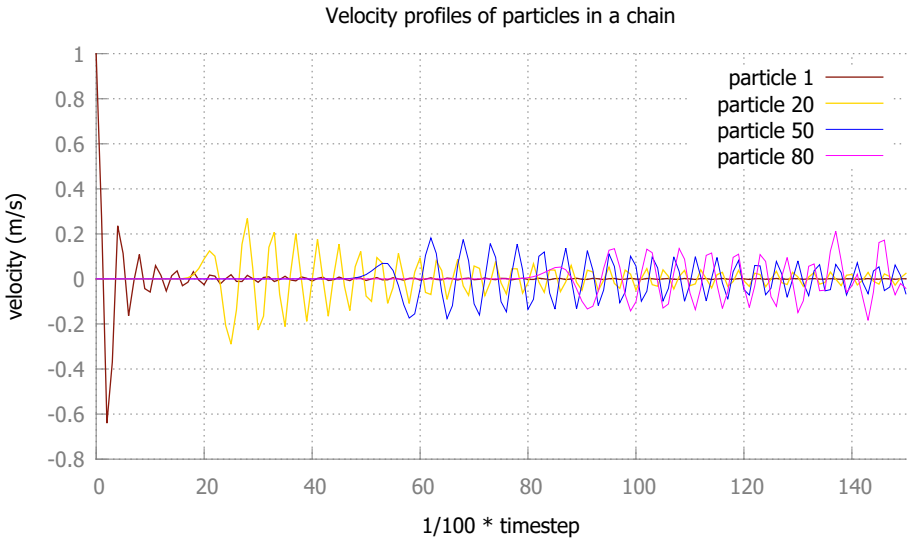

Figure 3.4.: The same plot as Figure 3.2 but with interparticle distance $d = -0.001$ [m]. The velocity profile no longer shows a peak for every single particle, but an oscillation. Not all momentum is therefore present in the wavefront.

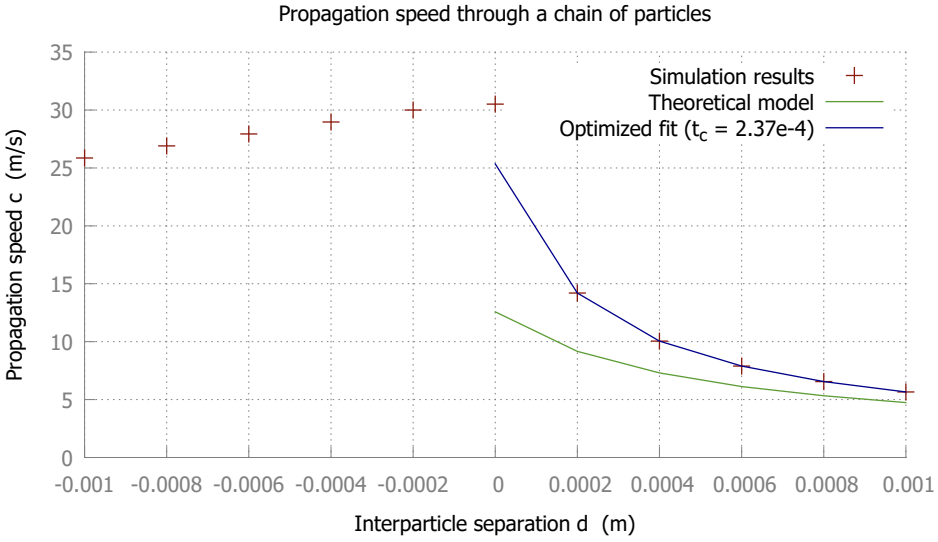

Figure 3.5.: Propagation speed for different interparticle distance. For a positive interparticle distance simple theoretical expression (Equation 3.1, with $t_c = 4.77 \times 10^{-4}$ [s]) can be fit. Note that at $d = 0$ the propagation speed changes quickly.

Setting	Symbol	Value	Unit
Number of particles	N	100	
Young's modulus	E	0.0014×10^9	[Pa]
Poisson ratio	ν	0.4	
Density	ρ	800	$[\mathrm{kg/m^3}]$
Radius	R	0.003	[m]
Cylinder thickness	h	0.003	[m]
Timestep size	Δt	$\frac{1}{5} \times 10^{-5}$	[s]
Initial velocity	v_0	1	[m/s]
Interparticle distance	d	varying	[m]

Table 3.1.: Simulation settings

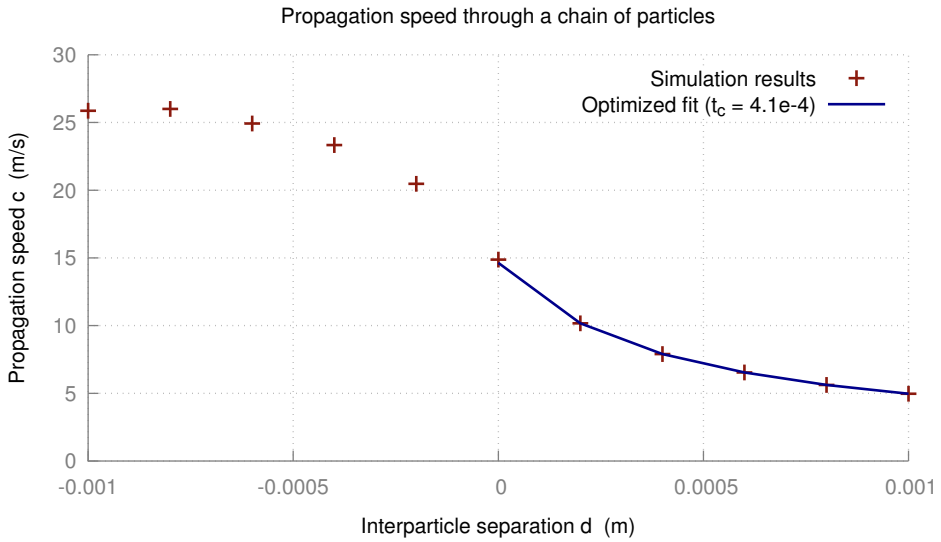

Figure 3.6.: The same figure as Figure 3.5 but with Hertzian spheres instead of disks. The fit shows a contact time of 4.1×10^{-4} [s], around a factor of 1.7 longer then Hertzian cylinders with the same material parameters.

Setting	Symbol	Value	Unit
Number of particles	N	20	
Timestep size	Δt	$\frac{1}{5} \times 10^{-7}$	[s]
Initial velocity	v_0	varying	[m/s]
Interparticle distance	d	-0.001	[m]

Table 3.2.: Simulation settings for varying initial speed. All settings are the same as Table 3.1 unless mentioned here.

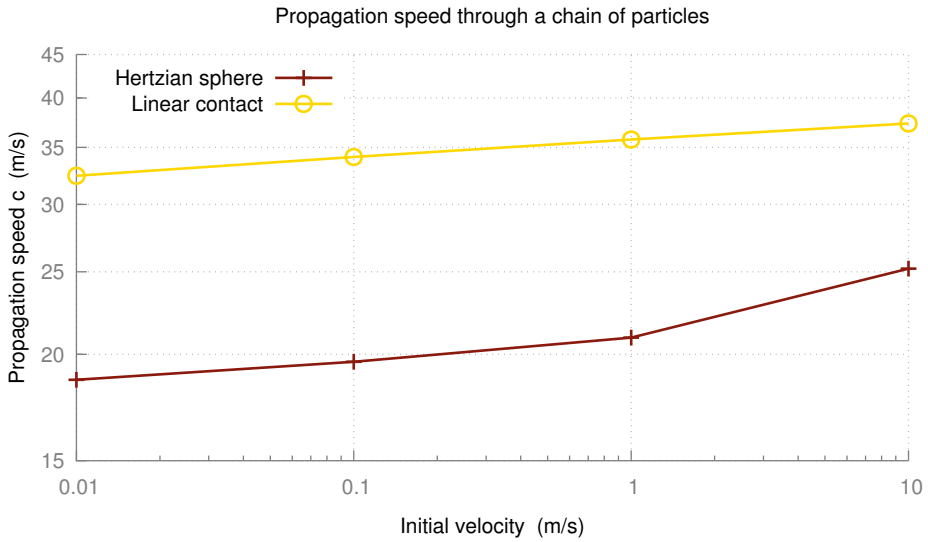

Figure 3.7.: Wave propagation speed in a simulation with different contact models (linear and a Hertzian contact model) for different initial velocities. Both particle types show an increase of speed with increasing initial speed.

3.2. On-ground experiments

3.2.1. Slow excitation using shaker

Initially the shaker was used as a way of exciting the granular packing as described in section 2.2. The shaker has however a maximum speed of 0.7 [m/s]. One can imagine that a very slow increase in pressure does not cause a significant wave front to develop, but is rather more like quasi-static loading. A high speed video[2] (recorded at a framerate of ca. 43000 per second, but slowed down in the online video) shows that indeed the packing shows quasi-static behaviour.

In the video the supposed wave is excited from the right and travels to the left. It is however clear when one looks at the left side of the image brightness slowly increases almost immediately (together with brightness on the right). There is no sign of a propagating wave front.

When looking at screenshots (not shown) one may be fooled easily because as the force chains propagate into the packing their intensity diminishes. On average the left parts of the image are therefore less bright and need more pressure to show up in the video. It may therefore appear as if a wave front is travelling anyway.

3.2.2. Typical results using a dropped weight

When instead of the shaker ran, a weight (m_1 in Table 3.4) is dropped (through a cylinder for guidance) the impact velocity is much higher. With the time to drop

$$t_{i,\text{drop}} = \sqrt{\frac{2h_i}{g}} \tag{3.5}$$

from a height of h_i and g the acceleration of gravity an estimation for the impact velocity can be found (disregarding air drag)

$$v_{i,\text{end}} = \sqrt{2gh_i}. \tag{3.6}$$

For a height of $h_4 = 39.85 \times 10^{-2}$ [m] the estimated end velocity $v_{4,\text{end}} = 2.80$ [m/s]. Whereas the shaker could achieve a maximum of 0.7 [m/s].

The higher impact velocity shows a much easier to identify wave front travelling. A typical result can be seen in a video online[3] or in the screenshots in Figure 3.8. Camera settings in all experiments are those of Table 3.3 unless mentioned otherwise.

A cylinder set upright above the sample cell with several cutouts to insert a weight provided a means to produce a repeatable experiment. The drop heights and masses of the weights are listed in Table 3.4.

After every drop the packing is slightly more compressed than before as friction prevents it from completely relaxing. To reinitialize the packing the top is taken off after every experiment and the packing is shaken until areas of high stress have relaxed. The

[2] https://kamphuisalex.stackstorage.com/index.php/s/fnrpsw4wJtBcLRt
[3] https://kamphuisalex.stackstorage.com/index.php/s/yFdTvloluw3VKls

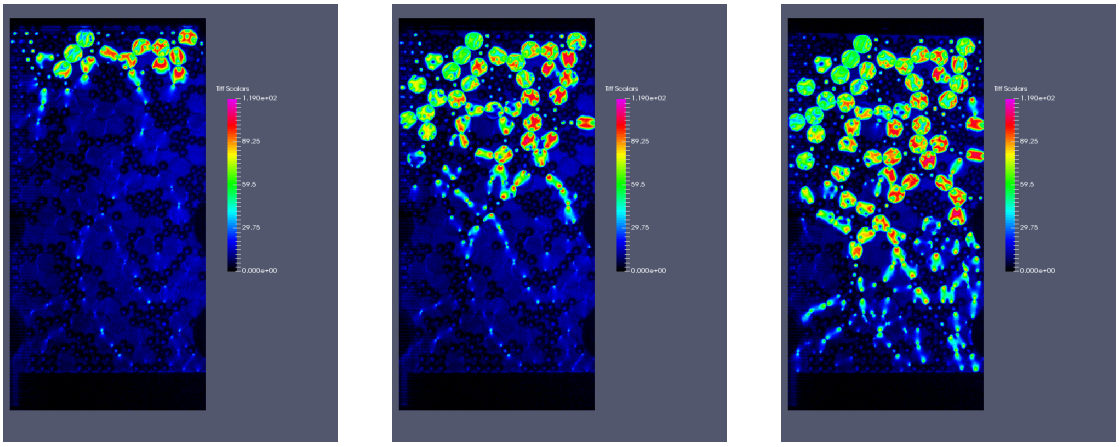

(a) frame 48 **(b)** frame 68 **(c)** frame 100

Figure 3.8.: Screenshots from a 40000 [fps] video when the weight hits our granular packing from a height of 39.85 [cm]. The three screenshots taken at different times clearly show the pressure wave travelling downwards at a finite speed.

Setting	Value	Unit
Frame rate	40000	[fps]
Shutter time	8	[μs]
Resolution	256×512	[pixels]
Image depth	8	[bit]

Table 3.3.: High speed camera settings

packing then expands and the top plate is reinserted. This produces a clearly defined packing at the start of every experiment (as inspired by personal communication with X. Jia, 10 Feb. 2016).

The time of flight for the wave is analysed by picking two rectangular areas of pixels with a height of 10 pixels across the complete width of the video frames. The intensity of all pixels in this area is summed for every timestep. As the wave arrives one expects a sharp increase in intensity in this area. This increase is shown in Figure 3.9.

It is very possible that after the arrival of the wave as apparent from the figure the pressure increases even further as the driver still moves slowly inward. This is consistent with existing work [70, 71].

The intensity of light that passes through a particle (in our circular polariscope) however saturates for increasing pressure (see subsection 3.2.5). It is therefore not feasible to relate the intensity of light to pressure directly. Other techniques exist and are still under development, see for instance [72, 73] but as they require high resolution images are not used here.

Parameter	Symbol	Value	Unit
Drop height 1	h_1	6.8×10^{-2}	[m]
Drop height 2	h_2	14.8×10^{-2}	[m]
Drop height 3	h_3	27.5×10^{-2}	[m]
Drop height 4	h_4	39.9×10^{-2}	[m]
Drop height 5	h_5	51.9×10^{-2}	[m]
Drop height 6	h_6	65.0×10^{-2}	[m]
Drop height 7	h_7	77.7×10^{-2}	[m]
Drop height 8	h_8	85.0×10^{-2}	[m]
Mass of top plate	m_0	29.2	[g]
Mass of weight	m_1	44.0	[g]
Mass of extra compression	m_2	280	[g]

Table 3.4.: Values of drop heights and masses of weights.

3.2.3. Non-linear wave propagation

Using a packing consisting out of ⌀3 [mm] spheres and ⌀6 [mm] disks/cylinders (with thickness/length 3 [mm]) several drops from different heights were filmed. The ratio of spheres to disks was so that both take up about 50% of the system area.

Each video of a drop gives one single sound propagation speed for that drop height. For every drop height the experiment was repeated 20 times and the averages and standard deviations plotted in Figure 3.10.

To the datapoints a powerlaw was fitted with a slope of $\frac{1}{6}$ in the double logarithmic plot using SciPy. For references on fitting using SciPy see [74, 75, 76]. In a similar experiment by van den Wildenberg [4] a similar power-law scaling was found.

Figure 3.11 shows average and binned data of velocity measurements for a single drop height. Even with a relatively low amount of data points (35 in this case) the onset of a Gaussian distribution is visible. The standard deviations shown in Figure 3.10 are rather significant but the averages seem to be easily fitted by the power-law. This may be explained that even though standard deviation in the data is ever present the average is (almost) independent of the number of data points. Although not completely proven the beginnings of the histogram in Figure 3.11 support this theory.

3.2.4. Particle type ratio differences

A similar experiment has been repeated with different packings consisting out of more spheres. The ratio's of spheres to disks 70/30 and 90/10 indicated in Figure 3.12 are taken so that 70% or 90% of the sample cell surface area is taken up by the spheres.

All packings show a similar slope in Figure 3.12 and the quantitative difference between the datapoints from one drop height is within error bars. Note that the soundspeed recorded is a lot lower then in Figure 3.10 because of the different method of time of flight determination. In this case the average arrival time was chosen as a measure for

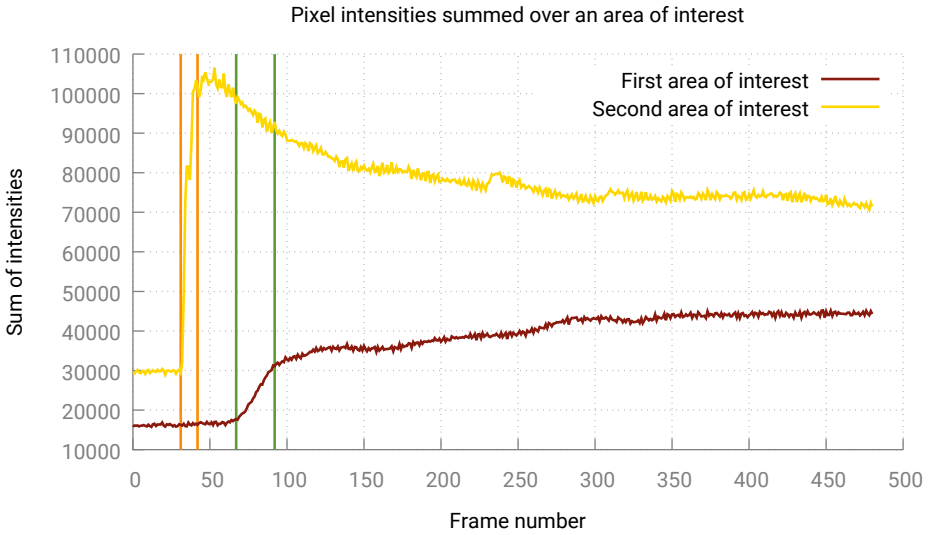

Figure 3.9.: Total intensity inside two areas of interest. Sharp increases (bordered with vertical lines) show the arrival of the pressure wave. Note that after the wave arrives pressure remains elevated but no longer increases.

arrival of the wave because as the ratio of spheres to disks increased the signal to noise ratio became smaller and made determination of the arrival time more difficult.

3.2.5. Precompression

As mentioned before the intensity of light transmitted through a particle saturates for higher pressures. To achieve an accurate measure for the pressure applied on a particle the number of fringes seen becomes important. The number of fringes can be related to the gradient of the intensity along a line pointing from particle center to contact [77, 78]. This technique requires a higher resolution because particle and contact positions need to be determined (and the resolution needs to be sufficient to capture all fringes).

However as the load on a particle increases it's fringe pattern does change leading to the suggestion that the difference between two consecutive images is a (al be it rough) measure for the pressure difference.

To investigate this possibility a wave was transmitted through a compressed packing. The video of the raw images[4] shows the wave travelling, however it is difficult to determine where the wave front is exactly at each frame. In the differential video[5] the absolute difference between two absolute frames is shown, making it much more clear how the wave travels. The same can be seen from the screenshots in Figure 3.13.

This technique (which was already used by Daniels [35]) is therefore promising for our setup but is not further used for this report.

[4] https://kamphuisalex.stackstorage.com/index.php/s/B6l6t5yLW1J9Dyy
[5] https://kamphuisalex.stackstorage.com/index.php/s/W0auwbnOMFI5Dfy

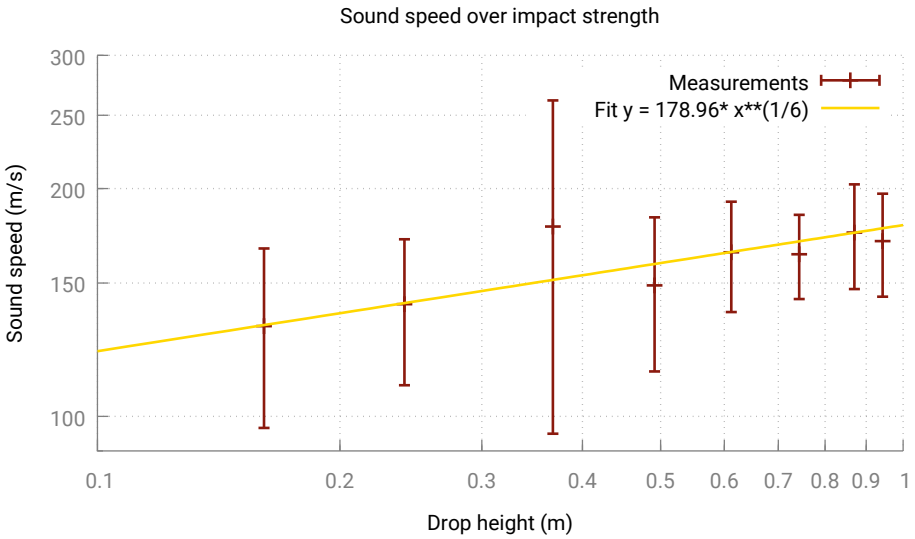

Figure 3.10.: Measured sound propagation speed for different drop heights (impact velocities). The datapoints are averaged over approximately 20 datapoints and the errorbars show standard deviations. A power-law was fitted and plotted (see text). Time of flight is based on the estimated arrival time of the wave (left lines of the pairs in Figure 3.9).

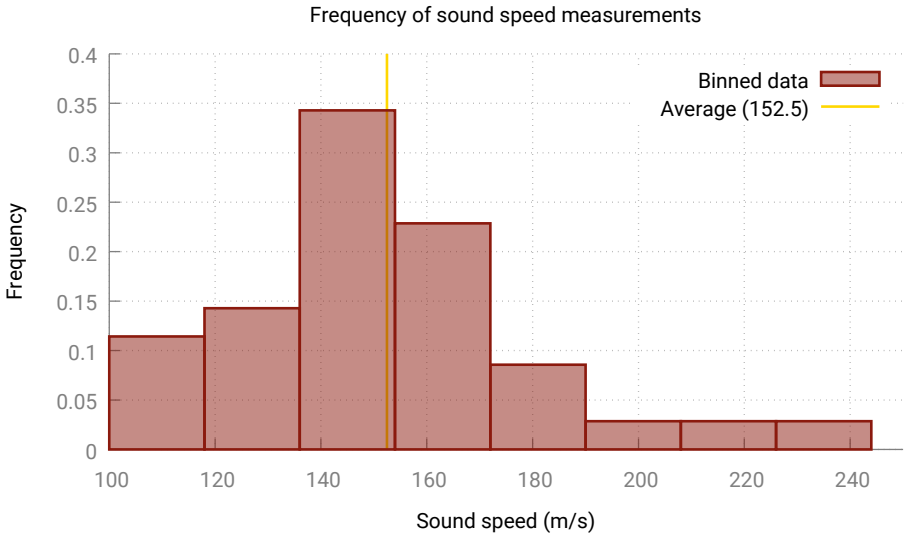

Figure 3.11.: 35 sound speed measurements binned to form a histogram. The height of the columns is the relative frequency for points within the width of a column. Note that roughly a Gaussian curve can be seen.

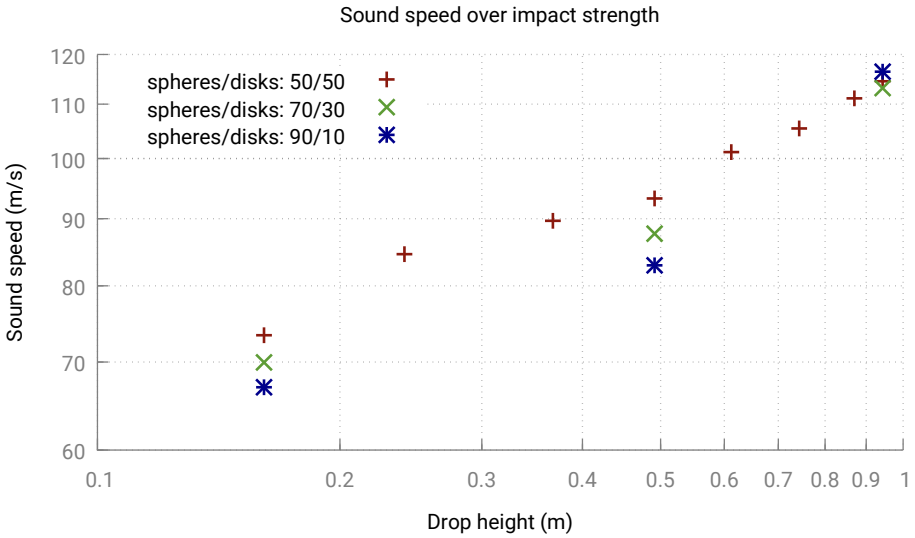

Figure 3.12.: Sound speed versus impact strength for packings of different ratios of particle types. The ratio is based on the amount of sample cell area taken up by that species. Note that the sound shows a similar slope in all cases. Time of flight was determined using the average arrival time (centerpoint between the line pairs in Figure 3.9). Power-law fit and error bars are not shown for clarity.

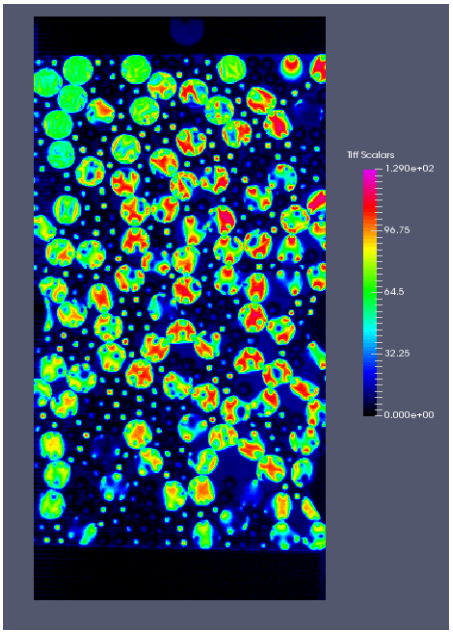

(a) Raw image, frame 33

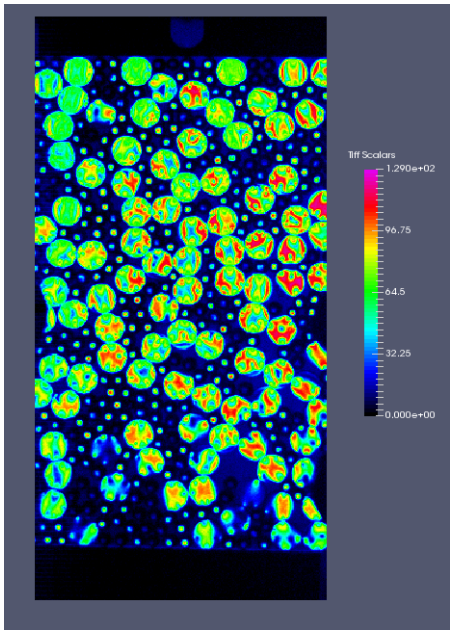

(b) Raw image, frame 45

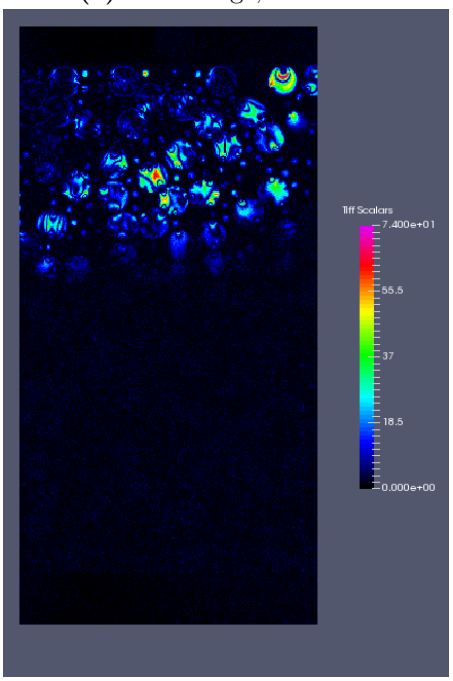

(c) Difference image, frame $|33 - 34|$

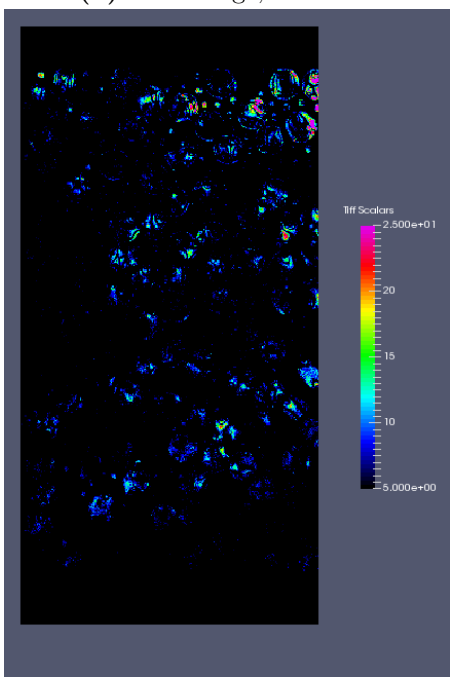

(d) Difference image, frame $|45 - 46|$

Figure 3.13.: Screenshots of a video showing a wave travelling through a precompressed packing. Using the top images (raw) the location of the wave is much more difficult to determine then using the bottom (differential) images.

3.3. Zero gravity experiments

3.3.1. On ground preparation

Using the device described in section 2.3 a blow (using the motor and hammer) is given to a granular packing. The blow then results in the propagation of a mechanical wave through the packing. In Figure 3.14 a typical sensor response is shown for a single wave. While filling the sample cell with particles the distance between the two sensors was recorded and using their responses a time of flight can be calculated as the difference of two arrival times. These two numbers combined give the propagation speed of the wave.

It is possible to define several points of interest on the sensor signal. The most obvious is hereafter called 'the peak' and is defined as the point at which the first sine-like wave has a peak and the peak's value. From there two half-height points can be defined traversing down from the peak, or other ratio's to the peak height. Given that the wave changes shape while propagating in an (for now) unknown manner the time of flight may show different behaviour depending on its definition. One definition is the difference between the arrival time of the peaks. Another would consist of the arrival time of a half-height point or even 20% height point. The closer to the first arrival of the wave one takes the point, the less influence by the shape-change of the wave but the more influence by the noise in the sensor data. A balance therefore needs to be found.

From each sensor response two numbers are extracted that are later plotted as dots in a graph like Figure 3.16. On the x-axis one finds a measure for the strength of the wave by taking the geometric mean (since the magnitude of both can vary greatly) of the peak heights

$$a_m = \sqrt{p_1 p_2}, \tag{3.7}$$

with a_m a measure for the amplitude of the wave and $p_{1,2}$ the height of the peaks converted to the unit of acceleration ($[\mathrm{m/s^2}]$) using the sensor's sensitivity.

In preparation of the in flight experiments tests have been performed to determine the difference between actuation via a moving wall as explained in section 2.3 (the wall is driven by the plunger listed there) or merely a plunger. The biggest difference is that the plunger has a limited size and thus creates a wave that one can easily imagine to spread to multiple directions, whereas actuation via a wall creates a plane wave (as far as this is possible in a granular medium). The typical results in Figure 3.15 qualitatively support this. In general the plunger actuated responses show additional small peaks and a plateau in the rise of the first large peak (especially for the far sensor).

One interpretation of this effect is that actuation via the wall causes several force chains to transmit a wave and the resulting signal is an average of the response through all these force chains. This averages out some irregularities like the plateau and the preceding small peak making it easier to describe the response. It was therefore decided to use a moving wall as actuation method because future analysis may be easier on the more smooth results.

Data acquired on ground, with the automatic hammer from section 2.3 replaced by a manual hammer, has been plotted in Figure 3.16. No linear regime can be seen (only

the non-linear regime with a slope of $\frac{1}{6}$ is visible) here which may mean the confining pressure was too low for these hammer strengths.

A higher confining pressure has been applied in Figure 3.17 that - possibly - shows a linear regime. Although hinting towards a linear regime the low number of data points at low wave amplitude is not yet convincing. The power-law fit however fits the data nicely beyond $a_m > 80$ [m/s^2].

3.3.2. In flight experiment

Pressure data

Figure 3.18 shows the pressure data during a single parabola. As supported by the data it is difficult to determine what the packing will be like during a $0g$ phase beforehand. In the case of Figure 3.18 the pressure sensors inside the packing drop to (near) zero during the no-gravity phase. For a packing to be well defined a non-zero pressure is desired because a zero valued pressure could also mean no particles are in contact. Consequently the pressure was gradually increased until a non zero value was measured during zero g phases.

Figure 3.19 shows the same pressure data across several (5) other parabolas. It is important to note that the pressure is now non-zero during the $0g$ phases and so the packing is considered well defined. It is however noteworthy that the pressure drops gradually (from parabola to parabola) indicating a rearrangement of the packing nevertheless. The rearrangement may be caused by repeated loading and unloading with gravitational force, by the repeated hammering, the vibrations coming from the aircraft or a combination thereof.

Number of data points

The amount of datapoints collected was limited by the 0g time (around 22 [s] per parabola) and the motor speed. The newly implemented software was (with limited resources available at the mini-PC) able to capture 10 data sets like the one visualized in Figure 3.21 per second (whereas existing software could only do 1 per second). The motor could provide circa 3 pulses per second. This gives a total of almost 6000 data points collected in 0g in a three day parabolic flight campaign.

The pressure data shows - amongst others - 0g phases where the pressure either drops completely to zero, or remains very high (> 1 [V]). We have however achieved several parabola's with a near uniform packing (in terms of pressure). The pressure data for one of such parabola's has been given in Figure 3.20. During the 0g phase in such a parabola the pressure throughout the packing is nearly uniform as signified by the three pressure values being very similar, whereas during the 1g phase the pressures are very different.

3.3.3. Acceleration data

Figure 3.21 shows a typical arrival signal for a wave collected in flight. The wave differs from the signals seen on ground (see Figure 3.14b) in that both signals often show two peaks. As the shape of the way may change during propagation through the packing it makes sense to select the very first rise as an arrival time. Currently a user-defined factor of the peak height has been used as a threshold for determining the arrival time. Selecting a suitable factor is non-intuitive as it as of yet unclear whether the first or second peak is most important (and what the difference between the two is).

Furthermore the added amount of noise from vibrations in the plane make it more difficult to detect with very low amplitudes. To overcome this a Butterworth low-pass filter [79] (with variable cut-off frequency) has been implemented.

A preliminary analysis has been performed on some of the data points that showed a non-zero pressure. Such an analysis is visualized in Figure 3.22. Due to the change in pressure from parabola to parabola as shown in Figure 3.19 it is difficult to draw quantitative conclusions from a figure like Figure 3.22. The rise in sound speed may be caused by higher confining pressure rather than the higher amplitude as witnessed on ground.

As the analysis of the data gathered is still in progress results will be published, together with data from a second parabolic flight campaign and two drop tower campaigns, elsewhere.

Displaced sensors

The change in packing (relaxation) indicated by this gradual pressure drop means that also the embedded acceleration sensors may have been able to move. From inspection after the flight (image not shown) it is clear that the sensors have remained in position (preserving the inter sensor distance) but they have rotated especially in the horizontal plane. Since the sensors are uni-axial this may cause a shift in perceived intensity of the wave.

Another test on ground has been performed with artificially rotated sensors to simulate the sensors having moved during zero gravity flights. The dataset shows nicely a linear regime and a power law fit at increasing wave amplitude, with possibly a transition region (between the two black lines) unused in the fitting.

The fact that the acceleration sensors have been moved artificially means that the value of the wave amplitude is now ‘unreliable’, but remains unchanged for every data point and thus can be used as index.

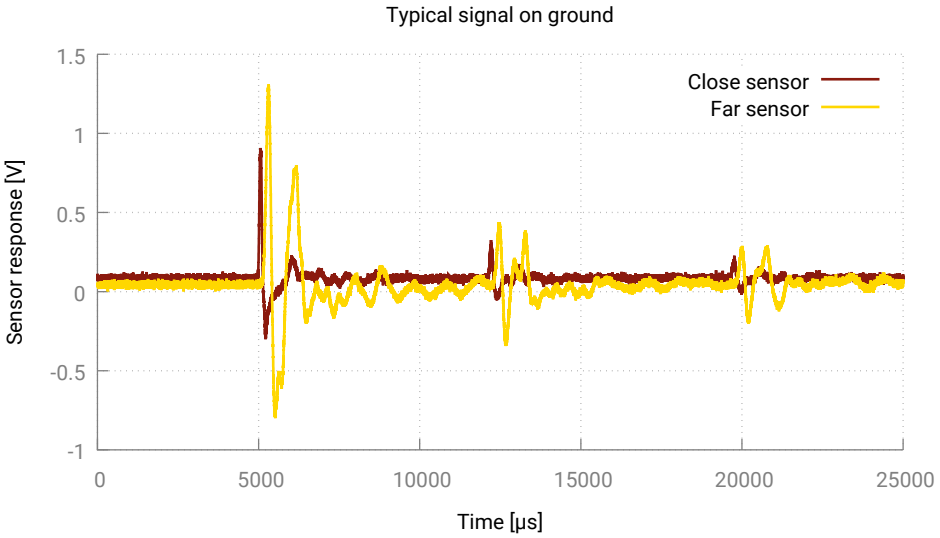

(a) The sensor response over a relatively large window of time (25 [ms]) showing clearly only noise in the beginning (up until ≈ 5000 [μs]), the arrival of the waves at that point (sharp peaks in both signals) and fluctuating signal after the arrival of the wave. This fluctuation may show signs of scattering and/or reflection but is not analysed in this report.

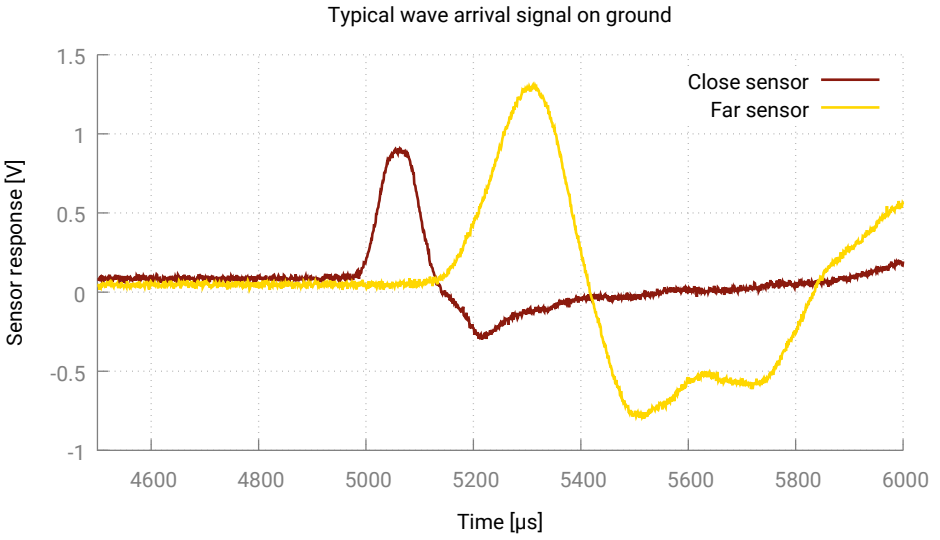

(b) Zoom in on the arrival of the wave for both sensors. The far sensor gives a stronger response in sensor voltage, because it is more sensitive (≈ 10 times more). Note that the shape of the wave is roughly similar for both sensors. Also note that after the first arrival peak a drop in sensor voltage occurs.

Figure 3.14.: A typical sensor response for an on-ground experiment.

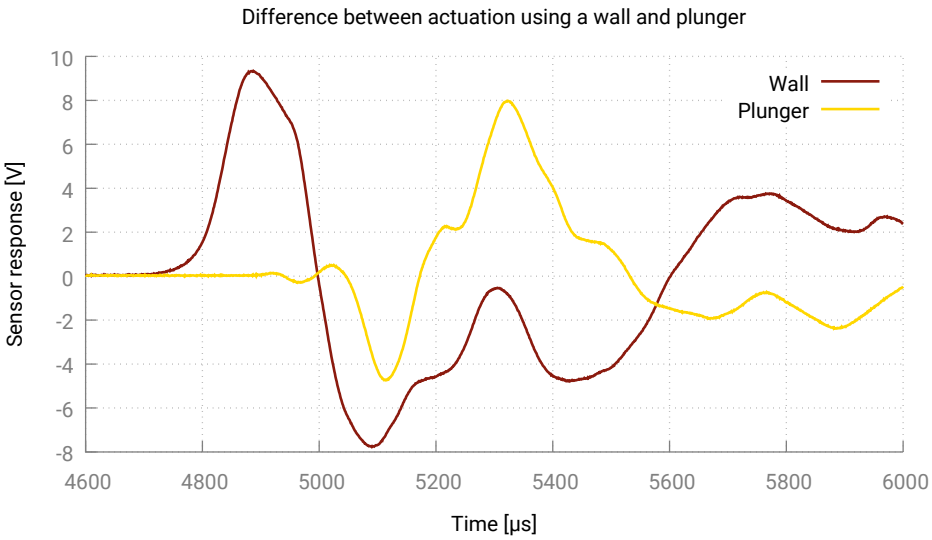

Figure 3.15.: Two typical sensor responses for the far sensor, one for actuation with a moving wall, and one for actuation with a plunger. Note how the signal for the plunger shows an early small peak (around 5000 [μs]) and a plateau in the rise of the large peak (around 5220 [μs]).

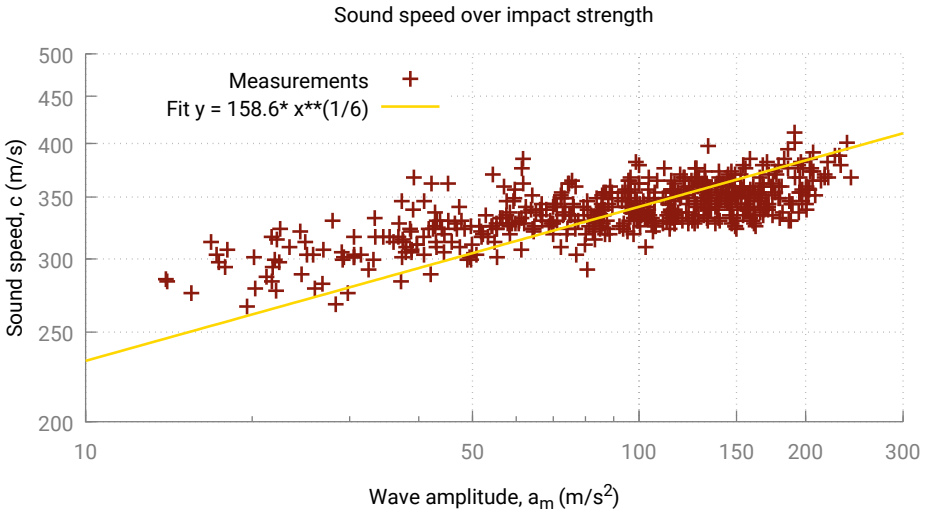

Figure 3.16.: A collection of data acquired on ground using a manual hammer. The sound speed shows a continuous increase across the entire data set, to which a $\frac{1}{6}$-power law has been fitted.

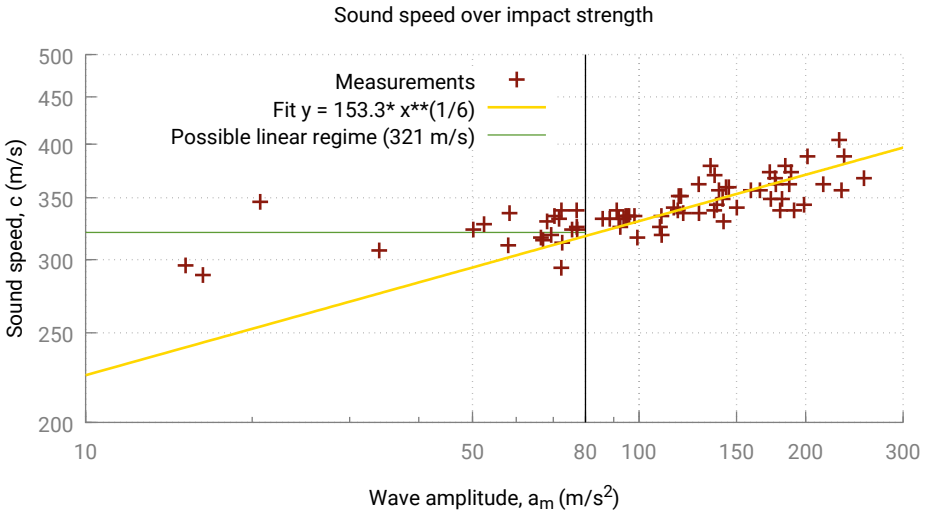

Figure 3.17.: Ground data from a manual hammering experiment with two fits. The first fit is a $\frac{1}{6}$ power-law fitted to the points where $a_m > 80$ [m/s^2] as indicated by the black vertical line. The second fit is a horizontal line at the average sound speed of the other points.

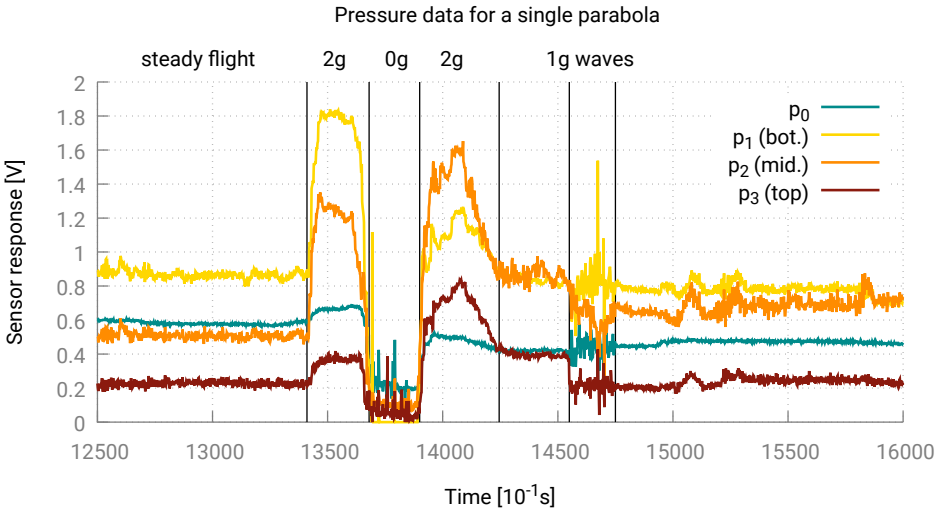

Figure 3.18.: Pressure data for a single parabola. Four sensors are shown of which p_0 is outside the the packing and measures the pressure on the moving wall. The others are inside the packing at different heights, p_1 being the lowest and p_3 the highest. Note how from the pressure data it is clear what phase of flight one is in (steady, 2g or 0g). An additional area is labelled '1g waves' because here experiments were conducted under steady flight conditions. The same spiky response is also seen during 0g when also experiments were run. The units on the vertical axis (Volts) are linearly related to the pressure measured via the sensitivity of the sensors which is yet to be determined.

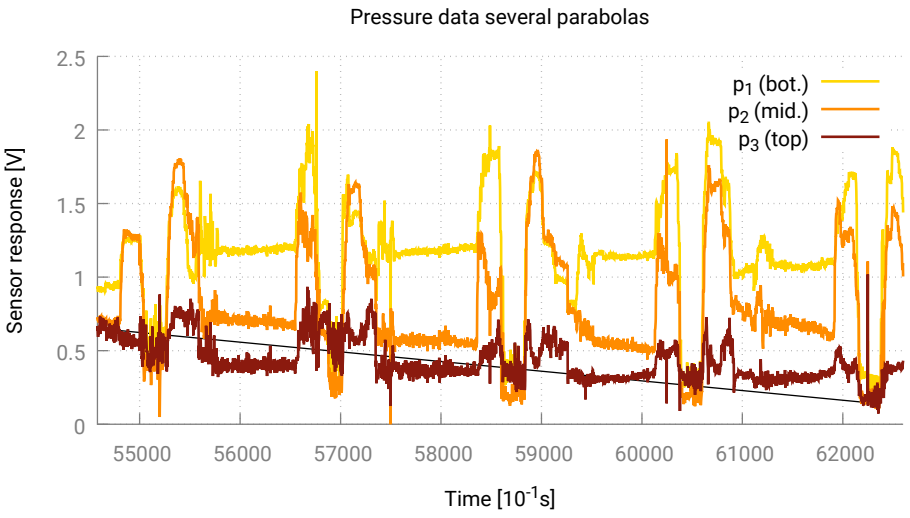

Figure 3.19.: Pressure data during 5 parabolas. Note how the pressure during the 0g phases drops gradually as indicated by the black line (drawn as visual aide). Data for the p_0 sensor is not shown since this sensor was disabled during these parabolas to avoid damage as a result of a high pressure.

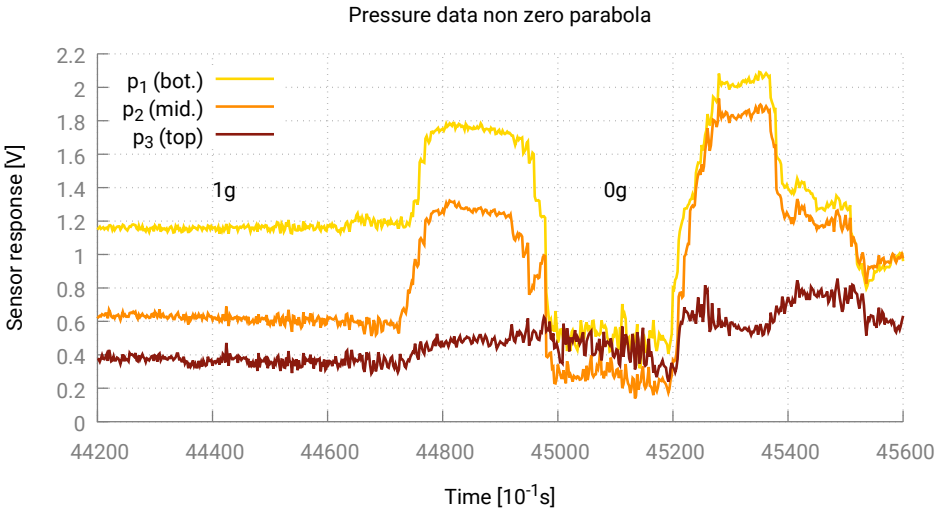

Figure 3.20.: Pressure data for a single parabola, where the pressure during the 0g phase did not drop to 0 [V]. Note that during the 0g phase the pressure is much more uniform throughout the packing than in the 1g phase before it.

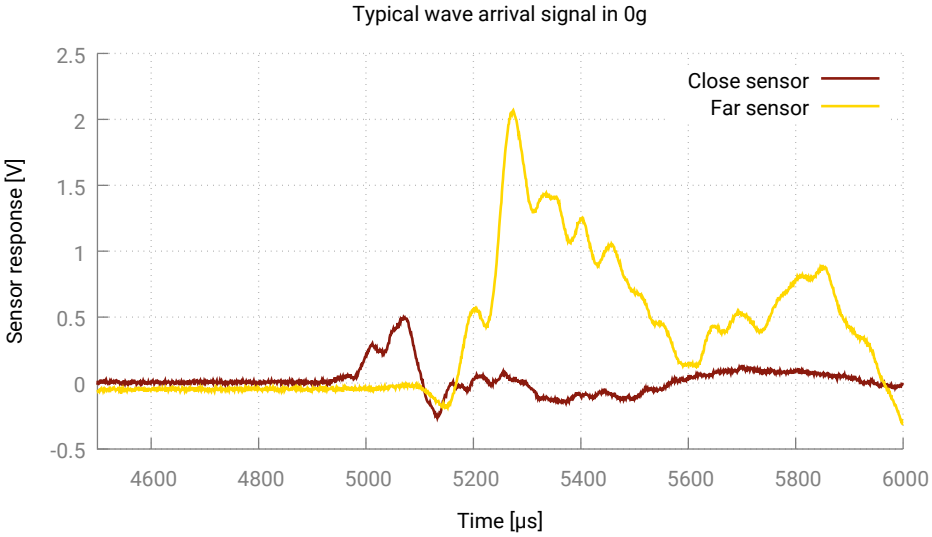

Figure 3.21.: Typical arrival of a wave in 0g. Note that the peak for both signals is rather dubious as there is a local maximum in the rising slope. Furthermore the far sensor appears to start with a drop rather than a rise in voltage around 5150 [μs].

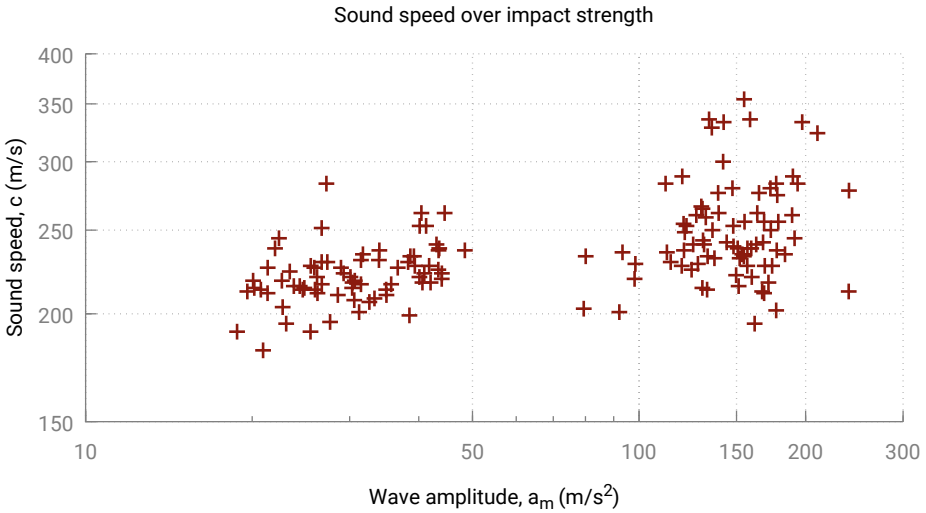

Figure 3.22.: Preliminary results from 0g phases with non-zero pressure. Data points are grouped in two distinct areas where the high wave amplitude points hint towards a slightly higher sound speed.

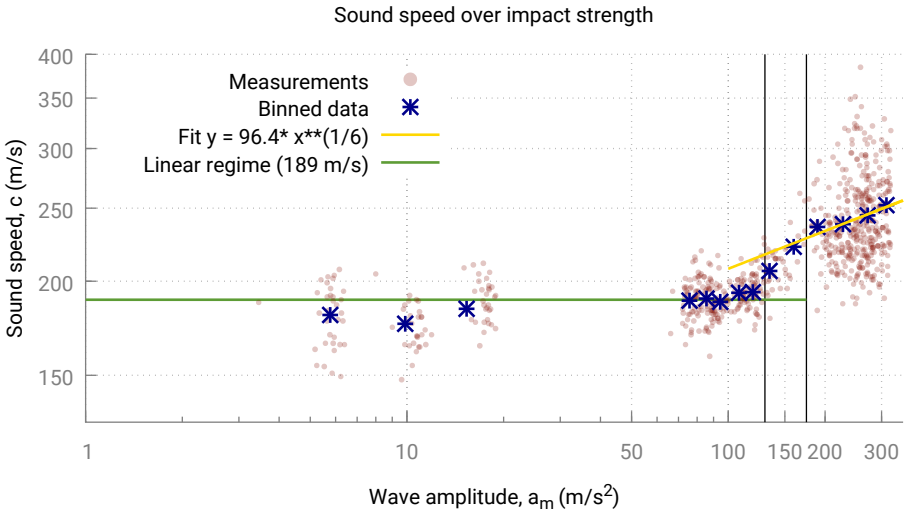

Figure 3.23.: On ground experiment with minimal confining pressure using the automated hammer and artificially displaced sensors (see text). Transparent red dots shows original data that has been binned into blue stars. To the data points for which $a_m > 175$ [m/s^2] a $\frac{1}{6}$ power-law has been fitted (yellow) as indicated by the rightmost black line. The fitted line corresponds nicely to the binned data. The average velocity for data points on the left of the leftmost black line is the linear regime (green line). This leaves two binned data points unused in any fit.

Chapter 4.

Discussion

This chapter discusses results presented before and combines the insights gained.

"In every outthrust headland, in every curving beach, in every grain of sand there is the story of the earth."

Rachel Carson

4.1. Simulation

Using a simplified granular system a set of one dimensional simulations has been run to analyse non-linear pressure wave propagation.

The formation of an unchanging propagating wave front can be seen clearly from the velocity profiles in Figure 3.2. The propagation speed of these wave fronts has been analysed for several confining pressures (related to the interparticle distance d) and shows behaviour as expected. See for instance Figure 3.5 where a theoretical model could nicely be fit to the simulation data.

The fit parameter - representing contact time t_c - found, was approximately two times smaller than the theoretically predicted contact time. Apparently particles interact faster than the typical contact time, but since the numbers are in the same order of magnitude and the qualitative behaviour is the same it can be argued the simulation fulfils theoretical expectations.

The non-linear behaviour for larger wave strengths could however not be replicated, not even with excitation speeds of several (10) meters per second. Both the linear contact model and Hertzian contact model for spheres show a very small power law relation between the wave propagation speed and initial excitation velocity v_0. Although the presence of this power-law clearly shows non-linear behaviour, it can in no way be compared to the $\frac{1}{6}$ power-law predicted. Gomez et al. [2, 3] have however shown the expected behaviour in simulations, leaving one to wonder what the differences are compared to our simulation presented in section 2.1. This question is also of physical relevance, as it explores the root cause for the non-linear behaviour.

Possible causes for the (lack of predictable) observed behaviour may be found in the excitation strength. Even if the initial inter particle overlap were converted to physical pressure units, it is currently unkown where the crossover between linear and non-linear behaviour happens. It is therefore possible that all simulations run are still within the linear regime and non-linear behaviour should not have been expected to begin with.

Gomez et al. [2] show via their mass balance (eq. 2) that the propagating wave front must have a velocity much higher then the particles themselves. As our particles are excited with a velocity that is in the same order of magnitude (10 [m/s]) as the propagating front ($\approx$ 20 [m/s]) the non-linear regime should already have been reached. Furthermore the material constants are similar to the materials used in section 2.2 where non-linear behaviour is easily visible for much lower excitation speeds ($\approx$ 2 [m/s]).

Perhaps the most striking difference between the simulations in literature and those in this report is the presence of disorder in literature. Our system is not only one dimensional (so only allowing for exactly one force chain and no particles outside that force chain) but also monodisperse (all particles have the same properties). Initial positions of particles were in all studied cases isotropic (the distance between particles was equal for all particles within one simulation).

Literature (i.e. Nesterenko [1]) predicts non-linear waves already in a one dimensional system that he solved analytically. Our simulation was unable to capture this behaviour which is striking since the system is very similar. One of the biggest differences in the methods used is the discretization of time in the case of the simulation. Molecular dynamic simulations become more accurate for smaller timestep sizes, and so part of the error may be attributed to a too large timestep.

The author however argues that the timestep size much smaller than the estimated contact time (50 times smaller) should be small enough to capture at least qualitatively the non-linear behaviour. This could be confirmed running simulations with smaller timestep sizes and comparison to results in section 2.1. The absence of the predicted non-linear sound propagation is therefore discussed more in section 4.4.

Another strong difference from the simulations performed by Gomez et al. [2] is the method of actuation. In our simulation a single particle within the packing is given an initial velocity so that it pushes against the others. This particle is the first particle of the packing, being that it separates the outside wall from the rest of the packing. In the case of Gomez a driver is used that moves forward with a constant velocity. Gomez et al. then also notice that most of the deformation of the packing happens behind the wave front which for us is not true.

The actuation method proposed by us is however rather close to the actuation in section 2.2 and section 2.3 where also a mass strikes with an initial velocity and is afterwards allowed to retract. There is a difference in ratio between particle and driver mass in simulation (where the ratio is 1) and experiment (where the ratio is $<< 1$) but the momentum transferred should still be enough at high enough initial velocities.

This leaves the important observation that qualitative behaviour in the cases investigated does not change for the Hertzian sphere contact model and the linear contact model as shown in Figure 3.7. Replacing the one with the other is therefore in at least the one dimensional case reasonable.

4.2. On-ground experiments

To find if a two dimensional setup with three dimensional particles can be used to study non-linear wave propagation several wave fronts were visualized using stress birefringent techniques and recorded using a high speed camera. Different mixtures of spheres and disks have been used.

From Figure 3.10 an increasing sound speed can be seen with the expected $\frac{1}{6}$ power-law. No linear regime was witnessed, possibly due to the strong excitation. With the current setup it is possible to excite less strong waves to find the linear regime.

Furthermore changing the ratio of spheres to disks does not qualitatively change the results as shown by Figure 3.12 that shows nearly the same sound speed and slope for all cases.

It is possible that the pressure waves travels faster through the spherical particles. In that case increasing the amount of spheres in the packing does not result in a change of sound speed, as witnessed in our experiment.

It has however already been argued that pressure waves travel preferentially along force chains [27, 35] and from visual inspection of the packings disks are very clearly part of force chains in some cases. If one would like to be more certain that disks do not change the behaviour witnessed different experiments with a larger number of disks could be run. The author expects similar results.

Upon changing the ratio of number of spheres to number of disks also the average particle size has been changed. The average size of the particles can surely influence the sound speed as it influences directly the amount of contacts a pressure wave must travel through per unit length in the propagation direction.

The change in number of particles (and thus contacts) per unit length should however not influence the expected power-law behaviour. It may cause an offset to the propagation speed (which was not observed) but one expects the same non-linear behaviour as was witnessed. Even more so, the different type of material (material properties of disks and spheres differ slightly, see Table 2.1) may also cause a different prefactor in the contact model, but this can only cause an offset to the sound speed found. Comparing the non-linear behaviour of different packings is therefore still valid.

If one would like to do more research to confirm the above it is possible to repeat the experiment with larger spheres and smaller disks, replace some of the spheres by disks, using only disks or a combination of these.

Furthermore it can be concluded that with the observation of non-linear wave propagation using the setup from section 2.2 additional research is very well possible. Upon augmenting the sample cell with (piezo- or acceleration) sensors to gain frequency information, making the sample larger to reduce boundary effects or suspending the particles in a frictionless environment to reduce friction additional accuracy may be gained.

4.3. Zero gravity experiments

To find possible points of improvement for the full three dimensional parabolic flight setup data, gathered with newly developed software tools, was analysed.

The new software proved much more effective and efficient then existing software in collecting data as it could, with the limited resources available, collect data points at a frequency 10 times higher than the existing software. The slowest process in the data collection chain is now no longer the software but the hammering mechanism (hardware).

During experimentation and analysis several problems have been identified, the problems and possible solutions are given below (section 4.3).

It may be argued that the accelerometers used are too big. Their surface area is several particle diameters (in each linear dimension). It is therefore possible that the sensors will not react much like the particles at all. The author argues that the larger surface area of the sensor will act as an average across several moving particles and reduce the number of measurements required to get a sense of bulk behaviour of the medium. Only when looking for inhomogeneity in the wave propagation a smaller sensor to particle diameter is needed.

As visible from the drop in pressure from parabola to parabola in Figure 3.19 it is very likely that the packing is not relaxed in at least the first parabolas. This may produce irreproducible results as the initial state of the packing varies from experiment to experiment. This is a difficult to solve problem because 0g times are very short. For now the 22 [s] of 0g time is all that is possible but the German Aerospace Center is working towards a sounding rocket and International Space Station mission that will allow for longer 0g times (several minutes and up) and so a more relaxed packing.

Using the data gathered already several other interesting phenomena may be studied. In principle it is possible to study attenuation, changing of the wave shape (broadening) and frequency behaviour. For the latter additional piezoelectric sensors may be put into the packing as they can be more accurate at small strain and high frequency.

Furthermore it is very well possible that the waves witnessed consist out of a linear and a non-linear part that due to the difference in their propagation speed will separate. A larger sample should make it easier to separate a 'slow' linear wave from jitter behind the non-linear wave front given that the excitation is strong enough. Alternatively it may be possible to reflect the wave on the boundaries of the sample cell to effectively create a longer path.

From here on the data gathered will be matched to pressure data to account for change in propagation speed as a result of confining pressure before combining the information from several parabolas into one bigger plot like Figure 3.22. Assuming the results are promising future work will aim towards scattering phenomena aboard rockets and International Space Station.

Points of improvement

Even though the hammer system allows setting the hammer speed with a very high resolution the resulting data points are found grouped around certain intensities (see for

instance Figure 3.23). Ideally the experimenters would like a more continuous continuous increase of hammer strengths to be able to track down the turning point between linear and non-linear regimes. Furthermore the current hammer system is controlled by feed-forward only, and this proved unstable during longer periods of experimentation sometimes resulting in the loss of data points during scarce 0g time. A hammer system with feed-back control specifically designed to hit the sample cell at specified speed may solve the problem. During the rest of the project such a solution will be sought.

As mention in section 3.3 the acceleration sensors have rotated (mainly in the horizontal plane) making it impossible to compare wave amplitudes from one set of parabolas to another. A possible solution would be to fix the sensors with wires to the sample cell walls or to use tri-axial sensors.

Most time during the parabolic flight was spent achieving the desired well-defined (but uniform) packing. As it was difficult to predict the state of the packing during a 0g phase beforehand multiple of such phases were used to find a sufficient confining pressure. The confining pressure was controlled by the amount of particles in the sample cell and the volume of the sample cell (by the moving wall). In granular media the relation between volume and pressure is not straightforward and so it makes more sense to control the pressure electrically. A linear actuator could control the moving wall getting feedback from the pressure sensors inside the packing. This would remove the need of manually changing the volume and greatly increase the number of useful datasets.

4.4. Combination

The main question raised when comparing the simulation to the two dimensional ground experiment is that of the difference in sound speed. The simulation shows a speed (around 20 [m/s]) much lower than the expected value (around 60 [m/s]). In comparison the on ground experiments show a speed much higher (at least 70 [m/s]) than the expected (around 50 [m/s]).

This leads one to wonder where the difference in behaviour originates. The first difference is the actuation method. In simulation a single particle is excited with a velocity v_0. This particle has a mass equal to all other particles whereas for the 2D experiment the plunger has a much bigger mass (around 100 particles, but it excites around 10 particles). This causes an increased per particle momentum.

It is possible that the lack of momentum in simulation causes a linear response rather than a non-linear response as seen in the 2D ground experiment, account for a difference in propagation speed.

Furthermore the contact models used in the simulation are most probably not suitable for wave propagation in soft materials. The first reason being the large strains these materials show and the second being the increased stiffness for higher frequencies. It may therefore be argued that the simulation is actually much closer to the three dimensional case where a propagation speed lower than expected is witnessed. Additional simulations with parameters for glass could be run to confirm this theory.

The last difference is the presence of disorder in all systems but the simulation. The

one dimensional nature of the simulations run can not account for complex behaviour such as the formation and breaking of force chains that will surely attribute to non-linear behaviour. Two dimensional simulations would therefore be more probable to show the expected behaviour as shown by Gomez [2].

Chapter 5.

Conclusion

> "The more sand has escaped from the hourglass of our life, the clearer we should see through it."
>
> *Johann P.F. Richter, 1795*

This chapter concludes the work presented. Theory and existing literature predict a $\frac{1}{6}$ power-law relation (non-linear regime) between wave propagation speed and wave amplitude (for sufficiently large wave amplitude at sufficiently small confining pressure only) and this phenomena has been studied using three different methods, amongst which a one dimensional simulation and two experiments of increasing complexity.

5.1. Simulation

Using a one dimensional molecular dynamics simulation a pressure wave was transmitted to a chain of particles. The particles interacted via a linear contact law or a Hertzian spherical contact law.

In both situations an unchanging wave front was found propagating at a fixed speed. For interpaticle distances larger than zero a theoretical model was fit predicting the propagation speed.

Afterwards the initial velocity (with which the wave is excited) was increased, but non-linear behaviour behaviour was not found to obey the $\frac{1}{6}$ power-law predicted. Instead a much smaller power-law 0.02 was found for both cases.

The cause for missing this specific behaviour may be found in the unjustifiable assumption of the contact models used (Hertzian spheres and a linear model) because the models will break down for soft particles. This is supported by the difference in magnitude of propagation speed in simulation which is much lower (20 [m/s]) than expected (ca. 60 [m/s]).

Qualitatively the behaviour is much closer to the linear regime in the three dimensional experiment with glass beads (which are much harder), because also here a slow down of the sound speed (with regard to the expected sound speed in an isotropic elastic medium) is witnessed, rather than a speed up.

Because also in the three dimensional experiment non-linear behaviour has been observed the simulation should in principle be able to capture this. So far the author has not succeeded in replicating this behaviour using the simulations presented. A stronger

excitation or increased disorder may be necessary to show the predicted behaviour.

5.2. On-ground experiments

Using different ratios of stress birefringent disks and spheres in two dimensional packings and a circular polariscope pressure waves have been filmed with a high speed camera. The pressure waves were initiated by a dropping weight.

The pressure waves originate as a wave front at the top of the packing (on which the weight is dropped). From there on they travel downward through the particles. The propagation velocity was estimated by estimating an arrival time based on the sum of all pixel intensities within an area of interest.

The propagation speed was plotted versus drop height on a log-log plot, showing an undeniable increase that has rather large errorbars. The approximate shape of the errors is Gaussian and so an average of the measurements were used to fit a power law with the predicted $\frac{1}{6}$ slope.

Changing the ratio of spheres to disks at three different drop heights does not directly show different behaviour. This supports the feasibility of using mixtures of stress birefringent spheres and disks as a medium to study non-linear wave propagation.

No linear regime was witnessed, possibly due to the strong impact strengths of the dropped weight. As dropping a smaller weight is trivial the author expects that finding the linear regime is very well possible with this setup.

5.3. Zero gravity experiments

Within a larger and ongoing project software tools have been developed to capture and analyse data from a three dimensional granular packing in parabolic flights.

A large number of data points has been collected on ground and during flight. Preliminary analysis shows that excitation using a moving wall rather than a plunger is more promising. Furthermore a non-linear regime has been witnessed on several occasions on ground.

Manually displacing the sensors to simulate the sensors having moved during 0g still shows the expected behaviour, including both linear and non-linear behaviour to which the *oneSixth* power-law could be fit.

Analysis of in flight data in general shows an increasing sound speed for higher wave amplitudes, but a more careful analysis is necessary (and ongoing).

Judging from pressure data gathered a packing much more uniform (in 0g) than in 1g has been achieved. The difficulty in achieving such a uniform packing is inherent to granular media but can be easier by implementing automatic pressure control of the sample cell (currently volume control is used). Additionally small changes to the setup have been proposed (such as feed-back controlled hammering mechanism and fixed accelerometers) to improve it.

5.4. Outlook

For further research the following notes and advice is given.

5.4.1. General

The power-law behaviour witnessed above is only part of the complete behaviour of the wave. To complete the picture additional insights are needed especially in the nature of the transition (if it is a transition at all) between linear and non-liner regimes. The speed of sound gives much more information on the packing if a precise description of the transition exists.

Furthermore other changes to the wave as it propagates to the packing need to be researched. One of the most obvious ones being attenuation. In this study no attention was paid to attenuation but it's existence is very clear. As the wave loses some of its energy as it propagates it is very well possible it also loses speed (because amplitude and velocity are related in the non-linear regime). Furthermore the attenuation will depend heavily on the contact and material properties so properly modelling it increases the effectivity of acoustically probing a granular packing.

Additionally the frequency specific behaviour of sound waves must be studied. Frequency will influence the propagation speed and attenuation and is key to the change of the shape of the wave as visible from our data (broadening).

On a more practical note it is necessary to settle on an accurate and above all unambiguous method of determining the arrival time of a pressure wave. As the wave changes shape it is non-trivial to compare two different arrival points. Finding such a method will rely also on frequency specific behaviour but will most likely have to be developed in parallel.

If the propagation of plane waves is fully described a next step must be the sideways scattering of a wave. As the origin of scattering is amongst others clearly the angle between particle contacts and the direction of propagation understanding scattering will provide information on the contact orientation.

Whereas compressional waves offer enough questions to study the behaviour above shear wave may offer new insights. If their behaviour is different from compressional wave it needs to be found why. If not, they offer an interesting platform as research. It may for instance be possible to submerge a granular medium in a density matching fluid so that effectively a microgravity environment is created. This does require a thorough understanding of the contact properties of wet granular matter.

5.4.2. Simulation

Simulation offers many advantages over experiment and so investing in simulation as a research tool is well worth the time.

To make the simulations described in this work useful in studying non-linear wave propagation first of all the non-linear propagation needs to be found. In order to do so one could increase the impact velocity or change the method of excitation.

A more systematic approach will add complexity to the simulation gradually moving towards a near-perfect description of a full three dimensional granular medium. As the behaviour of the packing changes upon adding complexities, such as increased disorder, more accurate contact models and higher dimensions, the influence of the last added feature can be studied. In parallel it would be necessary to study the combination of two or more of these features.

As demands on the simulation increase researchers must either develop the Pysim package further or use a different simulation tool for the work. Pysim offers ease of use for Python fans at the cost of a loss of execution speed and so may not be suitable for more complicated simulations.

Furthermore the small power-law witnessed in this report needs to be explained. If its grounds are physical this should be confirmed by experiment. Otherwise it's cause is numerical and therefore important for understanding and the development of Pysim or other simulation packages.

5.4.3. On-ground experiments

As this report has shown a potential for two dimensional setups with three dimensional stress birefringent particles further verification of the results is required.

It is crucial that more measurements are conducted to find if statistics offer a way of reducing the error size and to extend the range of the conclusions. Other ratios of spheres to disks may be used to study the properties of contacts and other size ratios may be used to study the importance of grain size.

Furthermore it is of vital importance that the linear regime is found in experiment so that the transition (if there is one) can be studied.

Methods to do so may involve a higher resolution in time (higher framerate for the camera) and space (higher camera resolution) as well as a larger system to further eliminate boundary conditions.

The two dimensional system really is the bridge between simulation and the full three dimensional complex system and offers unique ways of retrieving information. Extended experiments in two dimensions should for instance provide a validation or at least description of the contact of two particles during propagation of a wave, which may be fit into a simulation. Furthermore deriving the velocity and acceleration from visual position data allows to compare the two dimensional case to the three dimensional case which should give a hint of the role of the third dimension.

5.4.4. Zero gravity experiments

To make better use of scarce 0g time it is vital the experimental setup is improved. Areas of immediate focus should be automatic pressure control, a feedback controlled motor and fixed sensors. With the improved setup new data needs to be gathered. To increase repeatability of the experiment the packing likely needs to be relaxed making longer 0g times vital.

When a proper excitation method is implemented it is vital that the linear regime is found in flight and relate the transition between linear and non-linear regime to the confining pressure. Only then is it possible to systematically lower the confining pressure and investigate the limiting case of near zero confining pressure.

With the existing data a more thorough analysis can be done when each data point is related to a confining pressure at that point. Furthermore with the lack of an accurate amplitude measurement it is vital that data from one parabola is compared to the 2g and 1g phases near it because the sensors will probably have moved only little in this short time.

Appendix A.

List of symbols

Roman alphabet

a	Arbitrary constant
$\boldsymbol{a}_i$	Acceleration of particle i
a_m	A measure for the amplitude of a wave (geometric mean of peak heights)
A	Amplitude of a wave
c	Propagation speed of a wave
c_p	Propagation speed of a compressional wave
c_s	propagation speed of a shear wave
C	Strain optic coefficient
d	Differential operator
D_i	Diameter of particle i
$\boldsymbol{e}_i$	Unit vector in the x_i direction
E	Young's modulus (elastic modulus)
E^*	Effictive modulus of elasticity
E_i	Young's modulus for particle i
E_{kin}	Kinetic energy
E_{pot}	Potential energy
F	Force
vF_i	Force on particle i
$\boldsymbol{F}_{i(,j)}$	Force on particle i (by particle j)
[g]	one unit of gravitational acceleration (≈ 9.81 $\left[\text{m/s}^2\right]$)
G	Shear modulus
h	Height
h_i	Height i
k	Stiffness
k_i	Elastic (spring) constant of particle i
K	Bulk modulus
L	Length/height of a cylinder/disk
m	Mass
m_i	Mass of particle i
M	Compressional modulus

n	Timestep number
K	Stress optical coefficient
$\boldsymbol{n}_{ij}$	Unit normal vector pointing from $\boldsymbol{r}_i$ to $\boldsymbol{r}_j$
$\boldsymbol{O}$	Origin
p	Confining pressure
p_i	Height of peak number i
Q	$\frac{3}{4}\left(\frac{1-\nu_1^2}{\pi E_1}+\frac{1-\nu_2{}^2}{\pi E_2}\right)$
$\boldsymbol{r}_i$	Position of particle i
R	Radius
R_i	Radius of particle i
$S_{n,t}$	Normal and tangential stiffness
t	Time
u	Displacement/deformation
u_x	Displacement in the x direction
$\boldsymbol{v}_i$	Velocity of particle i
v_s	Propagation speed of a wave front
V	Volume
x	Spacial coordinate in the first linear dimension (x_1)
y	Spacial coordinate in the second linear dimension (x_2)
x_i	Cartesian coordinate i
z	Number of contacts for a particle
$\bar{z}$	Coördination number: average number of contacts per particle

Greek alphabet

α	Parameter to change the character of a wave equation
β	Porosity
δ_{ij}	Overlap between particles i, j
$\delta(x,t)$	Strain field value at x, t
$\delta_{s,0}$	Compression after and before a wave front
Δt	Timestep size
ε	Interaction parameter (depends on geometry and material properties)
θ_r	Angle of repose
κ	Complete elliptic integral of the first type
μ	One of the elastic moduli
ν_i	Poisson's ratio for particle i
ρ	Density
ϕ	Packing fraction (of volume or area, depending on dimensionality)
ϕ_j	Jamming point, the packing fraction at which (un)jamming occurs
ψ	Field governed by wave equation
ω	Angular frequency

Others

$\mathbf{0}$	zero vector
e	Eccentricity
$\mathcal{E}$	Complete elliptic integral of the second type
∂	Partial differential operator
$\boldsymbol{\nabla}$	Nabla, or the Del operator, defined by $\boldsymbol{\nabla} = \sum_{i=1}^{n} \boldsymbol{e}_i \frac{\partial}{\partial x_i}$ in n dimensions
$\varnothing$	Diameter

Appendix B.

Diametric loading of disks

In this appendix disks under diametric loading are considered. A schematic can be seen in Figure B.1.

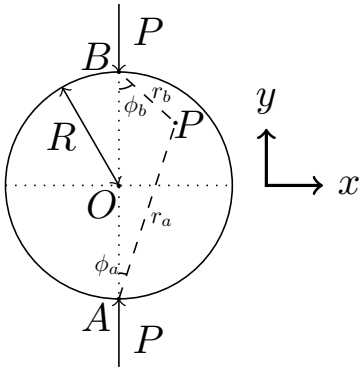

Figure B.1.: Schematic image of a disk with radius R under diametric loading. Forces are exerted at point A and B and cause a stress at point P which can be described in polar coordinates in three different coordinate systems. The (x, y) system is Euclidian and has its origin in point O. The other two system originate in points A and B and are described by polar coordinates (ϕ_a, r_a) and (ϕ_b, r_b) respectively.

B.1. Stress tensor

The stress distribution in a disk like this has been derived originally by Hertz [80] and is later used by Procopio et al. [81] to compare to experimental results. The nonzero elements of the stress tensor are (from Procopio)

$$\begin{aligned}
\sigma_{xx} &= -\frac{2P}{\pi t}\left(\frac{x^2(R-y)}{\beta_1^4} + \frac{x^2(R+y)}{\beta_2^4} - \frac{1}{2R}\right) \\
\sigma_{yy} &= -\frac{2P}{\pi t}\left(\frac{(R-y)^3}{\beta_1^4} + \frac{(R+y)^3}{\beta_2^4} - \frac{1}{2R}\right) \\
\sigma_{xy} &= \frac{2P}{\pi t}\left(\frac{x(R-y)^2}{\beta_1^4} + \frac{x(R+y)^2}{\beta_2^4}\right).
\end{aligned} \tag{B.1}$$

With L the thickness (or length) of the cylinder and $\beta_1^2 = (R-y)^2+x^2$, $\beta_2^2 = (R+y)^2+x^2$.

The matrix representation of stresstensor $\overline{\overline{\boldsymbol{\sigma}}}$ then has two nonzero eigenvalues corresponding to the two principal stresses. The third principal stress is identically zero since our problem is two dimensional. The principal stresses can be determined analytically but since their expressions are long writing them down here has no point. In stead a numerical representation using `Matlab` can be seen in Figure B.2.

Another representation can be found in a PhD thesis by Howell that follows the derivation in Theory of Elasticity by Landau and Lifschitz [82, 59]. This derivation does not assume small strain directly but still relies on Hooke's law in which parameters like the modulus of elasticity will change under extreme circumstances. The nonzero stresstensor components given are

$$\begin{aligned} \sigma_{r_a r_a} &= -\frac{2P}{\pi r_a}\cos(\phi_a) \\ \sigma_{r_b r_b} &= -\frac{2P}{\pi r_b}\cos(\phi_b) \\ \sigma_{ik} &= \frac{P}{\pi R}\delta_{ik}. \end{aligned} \tag{B.2}$$

Since the stresstensors are contravariant a transformation can be found with the use of the transformation rule

$$A'^{ij} = \frac{\partial x'^i}{\partial x^l}\frac{\partial x'^j}{\partial x^m}A^{lm}. \tag{B.3}$$

The first term of the complete tensor $\overline{\overline{\boldsymbol{\sigma}}}$ can be found by the transformation of $\sigma_{r_a r_a}$ to the (x, y) coordinate system:

$$\begin{aligned} \frac{\partial x}{\partial r_a} &= \frac{\partial r_a \sin(\phi_a)}{\partial r_a} = \sin\phi_a \\ \sigma^{xx} &= \frac{\partial x}{\partial r_a}\frac{\partial x}{\partial r_a}\sigma_{r_a r_a} + 2\frac{\partial x}{\partial r_a}\frac{\partial x}{\partial \phi_a}\cancelto{0}{\sigma_{r_a\phi_a}} + \frac{\partial x}{\partial \phi_a}\frac{\partial x}{\partial \phi_a}\cancelto{0}{\sigma_{\phi_a\phi_a}} \\ &= \sin(\phi_a)\sin(\phi_a)\sigma_{r_a r_a}. \end{aligned} \tag{B.4}$$

This can be done for all terms to find the three separate stress tensors in the new coordinate system,

$$\overline{\overline{\boldsymbol{\sigma_a}}} = \begin{bmatrix} s_a s_a & c_a s_a \\ c_a s_a & c_a c_a \end{bmatrix}\sigma_{r_a r_a} \qquad \overline{\overline{\boldsymbol{\sigma_b}}} = \begin{bmatrix} s_b s_b & c_b s_b \\ c_b s_b & c_b c_b \end{bmatrix}\sigma_{r_b r_b} \qquad \overline{\overline{\boldsymbol{\sigma_c}}} = \begin{bmatrix} 1 & 0 \\ 0 & 1 \end{bmatrix}\frac{P}{\pi R}, \tag{B.5}$$

with $s_{a,b} = \sin(\phi_{a,b}) = \frac{x}{r_{a,b}}$ and $c_{a,b} = \cos(\phi_{a,b}) = \frac{y\pm R}{r_{a,b}}$ that can be freely added together. The two descriptions differ only very slightly (a few percent) anywhere but close to the singular points at A and B and give an image like Figure B.2.

(a) **(b)**

Figure B.2.: Magnitude of the principal stresses in a particle with a radius and thickness of 1 [mm] when a force of 10 [N] is applied. *left:* principal stress 1 (σ_1) *right:* principal stress 3 (σ_3). Note that the second principal stress is identically zero.

Appendix C.

Birefringence and Retardation

C.1. Birefringence

The phenomenon of birefringence can be demonstrated relatively easily with the use of a calcite ($CaCO_3$) crystal, for instance as in Figure C.1. The double letters as seen through the crystal come from the fact that incident light in the crystal is randomly polarized. One can then express this randomly polarized light as two perpendicularly linearly polarized components. The components have a different refractive index n, the material is birefractive, and propagate at a different speed.

This difference makes for the fact that the two perpendicularly polarized beams travel in a somewhat different direction after refraction, showing the same letters twice.

The cause for birefringence differs for each material. In the case of crystals like calcite the cause lies in the anisotropic structure of the crystal. Other materials show birefringence because they consist of multiple materials or because of (residual) stress. In all cases however anisotropy is key.

Figure C.1.: A calcite crystal (Chemical formula $CaCO_3$) on a piece of paper so that the letters below can be read through the crystal. Note that through the crystal the letters appear double due to birefringence.

C.2. Retardation

The difference in propagation speed of light through a stress birefringent material can be used to probe the material for the internal stress state. An overview has been given by Howell in his PhD thesis [82] following a book by Durelli and Riley [83].

C.2.1. Case 1: Two linear polarizers and a sample

The case depicted in Figure C.2 shows the simplest setup for our problem. Linearly polarized light shines through the sample and a causes a phase shift that becomes measurable after a second linear polarizer. The intensity of the exiting light I depends on the phase shift α but also on the angle between the direction of polarization of the incoming light and the principal stress axes of the sample, θ in

$$I = I_0 \sin^2(2\theta) \sin^2\left(\frac{\alpha}{2}\right), \tag{C.1}$$

where I_0 is the intensity of the income light. To avoid this θ-dependence a slightly more complicated but similar setup can be used.

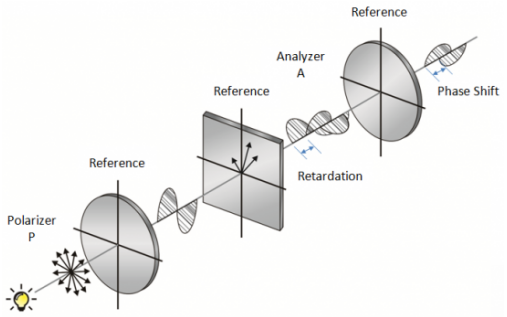

Figure C.2.: Two linear polarizers (the disks) show how an initial randomly polarized light beam (left) becomes first linearly polarized before travelling through a birefringent sample (middle, square plate). Afterwards the light beam can be decomposed in two perpendicularly polarized components with a phase shift. The second linear polarizer, shifted 90° to the first polarizer, effictively subtracting the two components. Two phase shifted parts remain (right). Image from [84].

C.2.2. Case 2: Two circular polarizers and a sample

This setup using two circular polarizers can be seen in Figure C.3. An explanation of exactly what happens has been given by Howell and by Durelli and Riley so is omitted here. One should just note their final expression for the light intensity after the second polarizer

$$I = I_0 \sin^2\left(\frac{\alpha}{2}\right), \tag{C.2}$$

with I the intensity of the light after the device, I_0 the incoming intensity and α the phase shift or retardation. Note that this was also already described by Frocht [85].

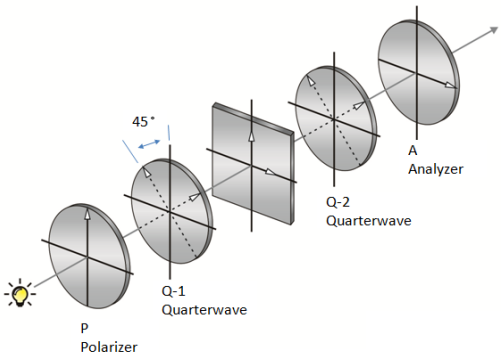

Figure C.3.: Circularly polarized light, made by passing linearly polarized light through a quarter wave plate, is passed through a sample (centre, square plate). The resultant beam can be decomposed along the principal stress axes of the sample after which a second quarter wave plate combines with the second linear polarizer to make a right hand polarizer. This effectively subtracts the two components in the direction of the last linear polarizer so that only the phase-shift remains. Image from [84].

C.3. The disk problem

Using the stress distribution from Appendix B and the formula's above one needs only the stress optic equation

$$R_t = Ct(\sigma_1 - \sigma_2) \tag{C.3}$$

with R_t the retardation, C the stress optic coefficient and $\sigma_{1,2}$ the principal stresses, to create a model for the light intensity through a diametrically loaded disk (because the phase shift α relates to R_t linearly: $\alpha = \frac{R2\pi}{\lambda}$, with λ the wavelength of the light). The model can then be fitted to experimental observations to find an expression for the forces a material is subject to. This has been done many times, for instance in [86, 77, 78, 87].

Simple cases have long been researched, see e.g. Frocht (who gives many examples) [85]. For more complicated systems however, consisting of several particles in a granular system research is still ongoing (the interested reader should keep an eye open for the not yet finished PhD thesis by Pitikaris from the DLR).

Appendix D.

Projections used in Pysim

Below are explained some equations used in the Pysim DEM package.

D.1. Geometry

Planes in the Pysim packages are defined by a point $\boldsymbol{A}$ which the plane touches and an outward pointing unit normal $\boldsymbol{n}$.

Call any other point (for instance the position of a particle) $\boldsymbol{P}$. The projection of $\boldsymbol{P}$ on the plane is then a new point called $\boldsymbol{B}$. The situation is sketched in Figure D.1.

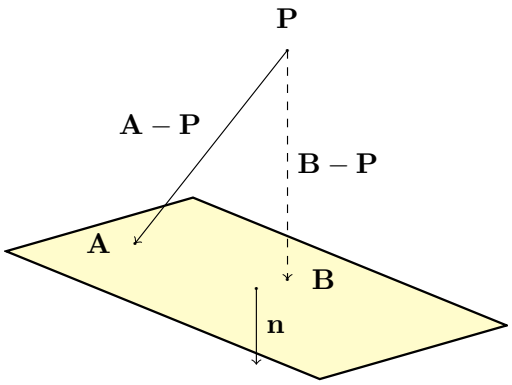

Figure D.1.: A plane defined by a point $\boldsymbol{A}$ and outward point normal $\boldsymbol{n}$ and a point $\boldsymbol{P}$, showing a line from point $\boldsymbol{P}$ to $\boldsymbol{A}$ and the projection $\boldsymbol{B} - \boldsymbol{P}$ to find point $\boldsymbol{B}$.

D.2. Vector pointing from point, normal to plane

The vector $\boldsymbol{B} - \boldsymbol{P}$ is the projection of the vector $\boldsymbol{A} - \boldsymbol{P}$ on the normal $\boldsymbol{n}$, multiplied by that vector and can be calculated using the dot product

$$\boldsymbol{B} - \boldsymbol{P} = [(\boldsymbol{A} - \boldsymbol{P}) \cdot \boldsymbol{n}]\boldsymbol{n}. \tag{D.1}$$

Distance The distance between point $\boldsymbol{P}$ and $\boldsymbol{B}$ is the absolute value of the projected length $|(\boldsymbol{A} - \boldsymbol{P}) \cdot \boldsymbol{n}|$.

Projection To find point $\boldsymbol{B}$ one can add the vector $\boldsymbol{B} - \boldsymbol{P}$ to point $\boldsymbol{P}$ so that

$$\boldsymbol{B} = [(\boldsymbol{A} - \boldsymbol{P}) \cdot \boldsymbol{n}]\boldsymbol{n} + \boldsymbol{B}. \tag{D.2}$$

Inside or outside A point is on the inside of a plane if a vector pointing towards the plane has a positive projected length on the outward pointing normal

$$\text{inside if: } (\boldsymbol{A} - \boldsymbol{P}) \cdot \boldsymbol{n} > 0 \tag{D.3}$$

$$\text{outside if: } (\boldsymbol{A} - \boldsymbol{P}) \cdot \boldsymbol{n} < 0. \tag{D.4}$$

The case where the projection equals zero occurs only when the point is on the plane.

Appendix E.

Hertzian contact models

The contact between individual grains in a granular packing is potentially difficult to describe. Due to asperities on the surface of a particle or inhomogeneities in shape or material properties a multitude of different configurations are possible for as little as two particles. In principle it is possible to model the interaction between two particles quite accurately (for instance using a Finite Element Model (FEM)) if all the necessary information (shape, material properties, pre-stress etc.) is known. In numerical simulations of a many particle system however this is computationally too expensive and in theoretical models this is too complicated. For this reason a two particle contact is often described by relating the overlap δ between two particles to the repulsive normal force f_n in molecular dynamics simulations (MD) or discrete element models (DEM) [44, 88].

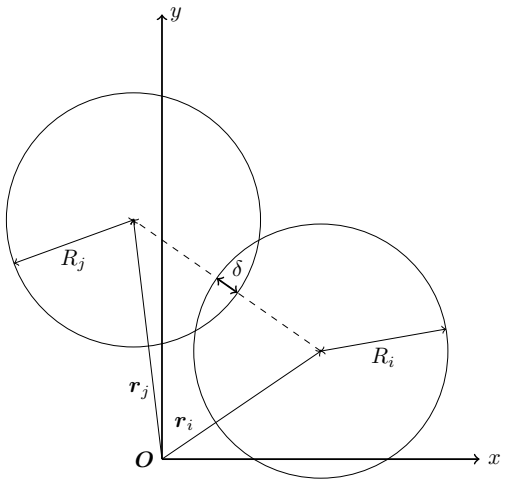

Figure E.1.: 2D view of two particles i, j with radius $R_{i,j}$ at $r_{i,j}$ in contact with overlap δ_{ij}.

A few assumptions can be made to arrive at a general description for the contact between two particles.

- Particles are either spherical or cylindrical.
- Particles are smooth, only forces normal to the plane of contact are considered.

- Particles are made of isotropic material.
- The material reacts linearly elastic.
- The interaction stays within the limits of this regime.

Using these assumptions the figure in Figure E.1 can be made. If furthermore is assumed that the contact surface is of the second order in shape a contact model known as the Hertzian model can be constructed. This was first done by Hertz [33] and an excellent rewrite of the derivation was made by Puttock and Thwaite [61] and Landau and Lifshitz [59]. For this report the relevant conclusions are

Sphere-Sphere contact

$$\delta = \left(\frac{9}{16RE^{*2}}\right)^{\frac{1}{3}} \cdot P^{\frac{2}{3}} \tag{E.1}$$

Cylinder-Cylinder contact

$$\delta = \frac{4}{\pi E^* L} \cdot P \tag{E.2}$$

Sphere-Cylinder contact

$$\delta = \kappa \left(2Q\right)^{\frac{2}{3}} \left(\frac{1}{R_1 \left(-\frac{1}{e}\frac{\mathrm{d}\mathcal{E}}{\mathrm{d}e}\right)}\right)^{\frac{1}{3}} \cdot P^{\frac{2}{3}} \tag{E.3}$$

The main source of non-linearity in the Hertzian contact models if found in the contact area. For an increase in applied force the compression (or overlap) must increase further deforming the objects pressed together. This deformation creates a contact area whose shape depends on the geometry of the objects. For the contact between two spheres the contact area is circular. A cylinder-cylinder contact is basically a rectangular contact so the contact area increases linearly with the force which is reflected by the linear relation between δ and P. The case of a sphere and a cylinder compressed together is very similar to two spheres pressed together with a correction for the elliptical shape of the contact area in the prefactor.

Note that these relations are approximations, and only as accurate as their initial assumptions, although their accuracy can be shown using for instance a FEM simulation in certain cases [89].

There is a qualitative difference between the relations for a sphere-sphere contact and a cylinder-cylinder contact found in the power law relation. Many studies have used spheres as a model granular media [11, 90, 91, 92, 30, 93] but when birefringent techniques are applied mostly disks are used [35, 82, 86, 27]. To my knowledge only the German Aerospace Center is currently able to use stress birefringent techniques in three dimensions [94]. Packings with spheres or disks both show rich behaviour but discussion is possible about whether disks copy the full complexity of the non-linear contact shown by spheres. It may be argued that asperities on the surface of disks and a slight misalignment of their central axes cause a non-linear interaction anyway. It is unclear in what compression range this applies.

E.1. Rewriting Puttock's notation

Puttock gives relations between compression and force (using other symbols than below). They can be rewritten as follows.

E.1.1. Sphere - Sphere

The expression for a contact between two spheres given by Puttock is

$$\delta = \frac{(3\pi)^{\frac{2}{3}}}{2} \cdot P^{\frac{2}{3}} \cdot \left(\frac{1-\nu_1^2}{\pi E_1} + \frac{1-\nu_2^2}{\pi E_2} \right)^{\frac{2}{3}} \cdot \left(\frac{1}{D_1} + \frac{1}{D_2} \right)^{\frac{1}{3}}. \tag{E.4}$$

Upon moving integers out of the power law and noting that π is both multiplied and divided by in equal powers one can write

$$\delta = \frac{1}{2} 9^{\frac{1}{3}} \pi^{\frac{2}{3}} \cdot \left(\frac{1-\nu_1^2}{\pi E_1} + \frac{1-\nu_2^2}{\pi E_2} \right)^{\frac{2}{3}} \cdot P^{\frac{2}{3}} \cdot \left(\frac{1}{D_1} + \frac{1}{D_2} \right)^{\frac{1}{3}} \tag{E.5}$$

$$\delta = \left(\frac{9}{8} \right)^{\frac{1}{3}} \cdot \left(\frac{1-\nu_1^2}{E_1} + \frac{1-\nu_2^2}{E_2} \right)^{\frac{2}{3}} \cdot \left(\frac{D_1 + D_2}{D_1 D_2} \right)^{\frac{1}{3}} \cdot P^{\frac{2}{3}}. \tag{E.6}$$

At which point the expression $1/E^* = (1-\nu_1^2)/E_1 + (1-\nu_2^2)/E_2$ is substituted

$$\delta = \left(\frac{9}{16} \right)^{\frac{1}{3}} \cdot \left(\frac{1}{E^*} \right)^{\frac{2}{3}} \cdot 2^{\frac{1}{3}} \left(\frac{D_1 + D_2}{D_1 D_2} \right)^{\frac{1}{3}} \cdot P^{\frac{2}{3}}. \tag{E.7}$$

Rewriting the diameters D_i as a function of the radius R_i gives

$$\delta = \left(\frac{9}{16} \right)^{\frac{1}{3}} \cdot \left(\frac{1}{E^{*2}} \right)^{\frac{1}{3}} \cdot \left(\frac{R_1 + R_2}{R_1 R_2} \right)^{\frac{1}{3}} \cdot P^{\frac{2}{3}} \tag{E.8}$$

and finally with substitution of $1/R = 1/R_1 + 1/R_2$

$$\delta = \left(\frac{9}{16 R E^{*2}} \right)^{\frac{1}{3}} \cdot P^{\frac{2}{3}}. \tag{E.9}$$

E.1.2. Sphere - Cylinder

For a sphere and cylinder contact Puttock writes

$$\delta = \frac{2QP}{a} \cdot \kappa \qquad\qquad a = \left(\frac{2Qp}{A} \right)^{\frac{1}{3}} \cdot \left(-\frac{1}{e} \frac{\mathrm{d}\mathcal{E}}{\mathrm{d}e} \right)^{\frac{1}{3}}, \tag{E.10}$$

which, upon substitution of a gives

$$\delta = \kappa \left(-\frac{1}{e} \frac{\mathrm{d}\mathcal{E}}{\mathrm{d}e} \right)^{-\frac{1}{3}} \cdot A^{\frac{1}{3}} \cdot (2QP)^{\frac{2}{3}}. \tag{E.11}$$

The force law can then be separated into a set of prefactors and the force P:

$$= \kappa \left(2Q\right)^{\frac{2}{3}} \left(\frac{1}{D_1 \left(-\frac{1}{e}\frac{\mathrm{d}\mathcal{E}}{\mathrm{d}e}\right)} \right)^{\frac{1}{3}} \cdot P^{\frac{2}{3}}, \tag{E.12}$$

where $Q = \frac{3}{4}\left(\frac{1-{\nu_1}^2}{\pi E_1} + \frac{1-\nu_2^2}{\pi E_2}\right)$ and κ and $-\frac{1}{e}\frac{\mathrm{d}\mathcal{E}}{\mathrm{d}e}$ are geometry depended constants that can be found using the tables provided by Puttock [61].

Bibliography

[1] V. F. Nesterenko. "Propagation of nonlinear compression pulses in granular media". In: *Journal of Applied Mechanics and Technical Physics* 24.5 (1983), pp. 733–743. ISSN: 00218944. DOI: 10.1007/BF00905892.

[2] L. R. Gómez et al. "Shocks near jamming". In: *Physical Review Letters* 108.5 (Feb. 2012), p. 058001. ISSN: 00319007. DOI: 10.1103/PhysRevLett.108.058001. arXiv: 1108.5688.

[3] L. R. Gómez, A. M. Turner, and V. Vitelli. "Uniform shock waves in disordered granular matter". In: *Physical Review E - Statistical, Nonlinear, and Soft Matter Physics* 86.4 (Oct. 2012), p. 041302. ISSN: 15393755. DOI: 10.1103/PhysRevE.86.041302. arXiv: 1208.0213.

[4] S. van den Wildenberg, R. van Loo, and M. van Hecke. "Shock waves in weakly compressed granular media." In: *Physical review letters* 111.21 (Nov. 2013), p. 218003. ISSN: 1079-7114. DOI: 10.1103/PhysRevLett.111.218003.

[5] O. Mouraille. "Sound propagation in dry granular materials : discrete element simulations, theory, and experiments". PhD Thesis. University of Twente, Feb. 2009, p. 135. ISBN: 9789036527897.

[6] M. Tsukahara. "Jamming in Granular Media: Modeling of Experimental Data". Phd Thesis. École Polytechnique Fédérale de Lausanne, 2009, p. 129. DOI: 10.5075/epfl-thesis-4490.

[7] J. R. Vaisnys and C. C. Pilbeam. "Mechanical Properties of Granular Media". en. In: *Annual Review of Earth and Planetary Sciences* 3.1 (May 1975), pp. 343–360. ISSN: 0084-6597. DOI: 10.1146/annurev.ea.03.050175.002015.

[8] T. Pöschel and S. Luding. *Granular gases*. Ed. by T. Pöschel and S. Luding. Vol. 564. Springer Science & Business Media, 2001, pp. 266–277. ISBN: 978-3-540-44506-7.

[9] J.-B. Michel et al. "Quantitative analysis of culture using millions of digitized books." en. In: *Science (New York, N.Y.)* 331.6014 (Jan. 2011), pp. 176–82. ISSN: 1095-9203. DOI: 10.1126/science.1199644. arXiv: NIHMS150003.

[10] H. L. Swinney and E. C. Rericha. "Pattern formation and shocks in granular gases". In: *Proceedings of The International School of Physics Enrico Fermi*. Aug. 2004, p. 34. arXiv: 0408252 [cond-mat].

[11] H. M. Jaeger and S. R. Nagel. "Physics of the Granular State". In: *Science* 255.5051 (1992), pp. 1523–1531. ISSN: 0036-8075. DOI: 10.1126/science.255.5051.1523.

[12] O. Reynolds. "LVII. On the dilatancy of media composed of rigid particles in contact. With experimental illustrations". en. In: *Philosophical Magazine Series 5* 20.127 (Dec. 1885), pp. 469–481. ISSN: 1941-5982. DOI: 10.1080/14786448508627791.

[13] G. Y. Onoda and E. G. Liniger. "Random loose packings of uniform spheres and the dilatancy onset". In: *Physical Review Letters* 64.22 (May 1990), pp. 2727–2730. ISSN: 00319007. DOI: 10.1103/PhysRevLett.64.2727.

[14] T. C. Hales. "Some algorithms arising in the proof of the Kepler conjecture". In: *ANNALS OF MATHEMATICS* 162.3 (2002), p. 14. ISSN: 0003-486X. DOI: 10.4007/annals.2005.162.1065. arXiv: 0205209 [math].

[15] S. Luding. "Granular matter: So much for the jamming point". In: *Nature Physics* 12.6 (Feb. 2016), pp. 531–532. ISSN: 1745-2473. DOI: 10.1038/nphys3680.

[16] R. L. Michalowski and N. Park. "Arching in Granular Soils". eng. In: *the First Japing - U.S. Workshop on Testing, Modeling, and Simulation*. ASCE, 2003, pp. 255–268.

[17] S. van den Wildenberg et al. "Soliton-like Shock Waves in Granular Materials". In: *Condensed Matter in Paris*. 2014.

[18] S. Luding. "Granular Media Information Propagation". In: *Nature* 435.7039 (May 2005), pp. 159–160. ISSN: 15393755. DOI: 10.1103/PhysRevE.73.035103.

[19] H. A. Janssen. "Versuche über Getreidedruck in Silozellen". In: *Zeitschr. d. Vereines Deutscher Ingenieure* 39.35 (1895), pp. 1045–1049.

[20] C. J. Reagle. "Technique for Measuring the Coefficient of Restitution for Microparticle Sand Impacts at High Temperature for Turbomachinery Applications". PhD thesis. Virginia Tech, Sept. 2012.

[21] H. Chen et al. "Enhanced granular medium-based tube and hollow profile press hardening". In: *CIRP Annals - Manufacturing Technology* 65.1 (2016), pp. 273–276. ISSN: 00078506. DOI: 10.1016/j.cirp.2016.04.010.

[22] O. Gendelman et al. "What Determines the Static Force Chains in Stressed Granular Media?" In: *Physical Review Letters* 116.7 (May 2016), p. 078001. ISSN: 10797114. DOI: 10.1103/PhysRevLett.116.078001. arXiv: 1505.06626.

[23] A. A. Peña, H. J. Herrmann, and P. G. Lind. "Force chains in sheared granular media of irregular particles". In: *AIP Conference Proceedings*. Vol. 1145. 1. AIP, June 2009, pp. 321–324. ISBN: 9780735406827. DOI: 10.1063/1.3179924.

[24] R. C. Hidalgo et al. *Force chains in granular packings*. 2004. DOI: 10.3254/978-1-61499-011-6-153.

[25] L. Zhang, Y. Wang, and J. Zhang. "Force-chain distributions in granular systems." In: *Physical review. E, Statistical, nonlinear, and soft matter physics* 89.1 (Jan. 2014), p. 012203. ISSN: 1550-2376. DOI: 10.1103/PhysRevE.89.012203.

[26] C. Song, P. Wang, and H. A. Makse. "A phase diagram for jammed matter". In: *Nature* 453.7195 (May 2008), pp. 629–632. ISSN: 0028-0836. DOI: 10.1038/nature06981.

[27] C. H. Liu and S. R. Nagel. “Sound in sand”. In: *Physical Review Letters* 68.15 (Apr. 1992), pp. 2301–2304. ISSN: 00319007. DOI: 10.1103/PhysRevLett.68.2301.

[28] E. W. Weisstein. *Wave Equation - 1-Dimensional - {http://tinyurl.com/wave-1d}*.

[29] X. Zeng, J. H. Agui, and M. Nakagawa. “Wave Velocities in Granular Materials under Microgravity”. en. In: *Journal of Aerospace Engineering* 20.2 (Apr. 2007), pp. 116–123. ISSN: 0893-1321. DOI: 10.1061/(ASCE)0893-1321(2007)20:2(116).

[30] M. Manjunath, A. P. Awasthi, and P. H. Geubelle. “Wave propagation in 2D random granular media”. In: *Physica D: Nonlinear Phenomena* 266 (Jan. 2014), pp. 42–48. ISSN: 01672789. DOI: 10.1016/j.physd.2013.10.004.

[31] S. Job et al. “Nonlinear waves in dry and wet Hertzian granular chains”. In: *Ultrasonics* 48.6-7 (Nov. 2008), pp. 506–514. ISSN: 0041624X. DOI: 10.1016/j.ultras.2008.03.006.

[32] N. P. Chotiros and M. J. Isakson. “Shear and compressional wave speeds in Hertzian granular media.” In: *The Journal of the Acoustical Society of America* 129.6 (June 2011), pp. 3531–43. ISSN: 1520-8524. DOI: 10.1121/1.3571421.

[33] H. R. Hertz. “Über die Beruhrüng fester elastischer Körper”. In: *Journal fur die reine und angewandte Mathematik* 92.156-171 (1882), pp. 156–171. ISSN: 0028-0836. DOI: 10.1038/055006f0.

[34] J. D. Goddard. “Nonlinear Elasticity and Pressure-Dependent Wave Speeds in Granular Media”. In: *Proceedings of the Royal Society A: Mathematical, Physical and Engineering Sciences* 430.1878 (July 1990), pp. 105–131. ISSN: 1364-5021. DOI: 10.1098/rspa.1990.0083.

[35] E. T. Owens and K. E. Daniels. “Sound propagation and force chains in granular materials”. In: *EPL (Europhysics Letters)* 94.5 (June 2011), p. 54005. ISSN: 0295-5075. DOI: 10.1209/0295-5075/94/54005. arXiv: 1007.3908.

[36] V. F. Nesterenko. “Nonlinear Impulses in Particulate Materials”. In: *Dynamics of Heterogeneous Materials*. New York, NY: Springer New York, 2001, pp. 1–136. DOI: 10.1007/978-1-4757-3524-6{_}1.

[37] E. Somfai et al. “Elastic wave propagation in confined granular systems”. In: *Physical Review E* 72.2 (Aug. 2005), p. 021301. ISSN: 1539-3755. DOI: 10.1103/PhysRevE.72.021301.

[38] V. F. Nesterenko. *Dynamics of Heterogeneous Materials*. New York, NY: Springer New York, 2001. ISBN: 978-1-4419-2926-6. DOI: 10.1007/978-1-4757-3524-6.

[39] C. Carpentier. “Three-dimensional visualization of contact networks in granular material”. PhD Dissertation. Universiteit van Amsterdam, 2013, p. 188. ISBN: 9789461918550.

[40] A. G. Athanassiadis et al. “X-ray tomography system to investigate granular materials during mechanical loading”. In: *The Review of scientific instruments* 85.8 (Aug. 2014), p. 083708. ISSN: 10897623. DOI: 10.1063/1.4893555. arXiv: 1406.2756.

[41] X. Lee, W. Dass, and C. Manzione. *Characterization of the Internal Microstructures of Granular Materials Using Computerized Tomography*. 1993.

[42] T. Kawaguchi. "MRI measurement of granular flows and fluid-particle flows". In: *Advanced Powder Technology* 21.3 (May 2010), pp. 235–241. ISSN: 09218831. DOI: 10.1016/j.apt.2010.03.014.

[43] H. Konietzky. "Numerical modelling in micromechanics via particle methods". In: (2003). Ed. by H. Konietzky, pp. 1–56.

[44] S. Luding. "Introduction to discrete element methods: Basic of contact force models and how to perform the micro-macro transition to continuum theory". In: *European Journal of Environmental and Civil …* Md (May 2008), pp. 785–826. ISSN: 1964-8189. DOI: 10.3166/ejece.12.785-826.

[45] A. Clement et al. "Comparing Numerical Integration Methods". In: *NM Supercomputing Challenge* (2008), p. 177.

[46] G. J. Martyna, M. E. Tuckerman, and D. J. Tobias. "Molecular Physics : An International Journal at the Interface Between Chemistry and Physics Explicit reversible integrators for extended systems dynamics". en. In: *Molecular Physics* 87.February 2015 (Apr. 1996), pp. 37–41. ISSN: 0026-8976. DOI: 10.1080/00268979600100761.

[47] H. Grubmüller et al. "Generalized Verlet Algorithm for Efficient Molecular Dynamics Simulations with Long-range Interactions". en. In: *Molecular Simulation* 6.1-3 (Mar. 1991), pp. 121–142. ISSN: 0892-7022. DOI: 10.1080/08927029108022142.

[48] R. Trobec and D. Janezic. "Comparison of Parallel Verlet and Implicit Runge-Kutta Methods for Molecular Dynamics Integration". In: *Journal of Chemical Information and Modeling* 35.1 (Jan. 1995), pp. 100–105. ISSN: 1549-9596. DOI: 10.1021/ci00023a014.

[49] M. J. Mikkola, M. Tuomala, and H. Sinisalo. "Comparison of numerical integration methods in the analysis of impulsively loaded elasto-plastic and viscoplastic structures". In: *Computers and Structures* 14.5-6 (Jan. 1981), pp. 469–478. ISSN: 00457949. DOI: 10.1016/0045-7949(81)90067-5.

[50] S. Luding. "Contact Models for Very Loose Granular Materials". In: *IUTAM Symposium on Multiscale Problems in Multibody System Contacts*. Vol. 1. Springer, May 2007, pp. 135–150. ISBN: 978-1-4020-5980-3. DOI: 10.1007/978-1-4020-5981-0{_}14.

[51] S. Plimpton. "Fast Parallel Algorithms for Short-Range Molecular Dynamics". In: *Journal of Computational Physics* 117.1 (Mar. 1995), pp. 1–19. ISSN: 00219991. DOI: 10.1006/jcph.1995.1039.

[52] B. R. Brooks et al. "CHARMM: A program for macromolecular energy, minimization, and dynamics calculations". In: *Journal of Computational Chemistry* 4.2 (Jan. 1983), pp. 187–217. ISSN: 0192-8651. DOI: 10.1002/jcc.540040211.

[53] J. C. Phillips et al. *Scalable molecular dynamics with NAMD*. Dec. 2005. DOI: 10.1002/jcc.20289. arXiv: NIHMS150003.

[54] D. A. Case et al. *The Amber biomolecular simulation programs*. Dec. 2005. DOI: 10.1002/jcc.20290. arXiv: NIHMS150003.

[55] S. Pronk et al. "GROMACS 4.5: A high-throughput and highly parallel open source molecular simulation toolkit". In: *Bioinformatics* 29.7 (Apr. 2013), pp. 845–854. ISSN: 13674803. DOI: 10.1093/bioinformatics/btt055.

[56] K. Bowers et al. "Scalable Algorithms for Molecular Dynamics Simulations on Commodity Clusters". In: *ACM/IEEE SC 2006 Conference (SC'06)*. IEEE, Nov. 2006, pp. 43–43. ISBN: 0-7695-2700-0. DOI: 10.1109/SC.2006.54.

[57] A. Thornton et al. "A review of recent work on the discrete particle method at the University of Twente: an introduction to the open-source package MercuryDPM". In: *DEM6 - International Conference on DEMs*. Colorado School of Mines, Apr. 2013, pp. 50–56. DOI: 10.1063/1.4812098.

[58] A. (A. C. Kamphuis. *PySim MD simulation - {pysim.alexkamphuis.nl}*. 2016.

[59] L. D. Landau and E. M. Lifschitz. *Theory of elasticity*. 1959. ISBN: 0-08-33917-4.

[60] S. Roux. "Quasi-Static Contacts". In: *Physics of Dry Granular Media*. Dordrecht: Springer Netherlands, 1998, pp. 267–284. DOI: 10.1007/978-94-017-2653-5{_}19.

[61] M. J. Puttock and E. G. Thwaite. *Elastic Compression of Spheres and Cylinders at Point and Line Contact*. Ed. by {Commonwealth Scientific and Industrial Research Organization}. Vol. 25. 25. Melbourne, 1969, p. 64.

[62] Vishay Company. *Vishay corporate website - http://www.vishay.com/*.

[63] S. Frank-Richter, M. Sperl, and P. Yu. *Producing spherical, stress-birefringent particles, comprises introducing a single- or multi-component solidifying liquid into a suspension liquid and removing the solidified particles from the forming slurry*. 2011.

[64] D. Weber. "Verfahren zur Optimierung Spannungsoptischer Analysen Dreidimensionaler Granularer Systeme". BSc. Thesis. Hochschule Bonn-Rhein-Sieg, 2015, p. 70.

[65] SilikonProfis. *Silikon Profis corporate website - {http://www.silikon-profis.de/ELBESIL-SILIKONOEL-B-60000-60000-cSt-500-g}*.

[66] S. Farhadi, A. Z. Zhu, and R. P. Behringer. "Stress Relaxation for Granular Materials near Jamming under Cyclic Compression". In: *Physical Review Letters* 115.18 (Oct. 2015), p. 188001. ISSN: 10797114. DOI: 10.1103/PhysRevLett.115.188001. arXiv: arXiv:1309.7147v1.

[67] J. H. Snoeijer et al. "Sheared force networks: anisotropies, yielding, and geometry." In: *Physical review letters* 96.9 (Mar. 2006), p. 098001. ISSN: 0031-9007. DOI: 10.1103/PhysRevLett.96.098001.

[68] Novespace, DGA, and M. d. l. D. R. Francaise. *PFC safety instructions*. 2016.

[69] L. de Mol. “Wave Propagation in Granular Material: Theoretical and Numercical Analyisis in Comparison to Experimental Data”. PhD thesis. Enschede: University of Twente, 2013, p. 99.

[70] S. van den Wildenberg, M. van Hecke, and X. Jia. “Evolution of granular packings by nonlinear acoustic waves”. en. In: *EPL (Europhysics Letters)* 101.1 (Jan. 2013), p. 14004. ISSN: 0295-5075. DOI: 10.1209/0295-5075/101/14004.

[71] X. Jia, T. Brunet, and J. Laurent. “Elastic weakening of a dense granular pack by acoustic fluidization: Slipping, compaction, and aging”. In: *Physical Review E - Statistical, Nonlinear, and Soft Matter Physics* 84.2 (Aug. 2011), p. 020301. ISSN: 15393755. DOI: 10.1103/PhysRevE.84.020301.

[72] T. H. Baek, M. S. Kim, and D. P. Hong. “Fringe analysis for photoelasticity using image processing techniques”. In: *International Journal of Software Engineering and its Applications* 8.4 (2014), pp. 91–102. ISSN: 17389984. DOI: 10.14257/ijseia.2014.8.4.11.

[73] J. Y. H. Lawrence. “Analyzing photoelastic disks”. PhD thesis. Reed College, 2012, p. 82.

[74] J. Eric, O. Travis, and P. Pearu. *SciPy : Open source scientific tools for Python*. 2001.

[75] K. J. Millman and M. Aivazis. *Python for scientists and engineers*. Mar. 2011. DOI: 10.1109/MCSE.2011.36. arXiv: MCSE.2011.36 [DOI:10.1109].

[76] T. E. Oliphant. “Python for scientific computing”. In: *Computing in Science and Engineering* 9.3 (2007), pp. 10–20. ISSN: 15219615. DOI: 10.1109/MCSE.2007.58.

[77] T. S. Majmudar and R. P. Behringer. “Contact force measurements and stress-induced anisotropy in granular materials.” In: *Nature* 435.7045 (June 2005), pp. 1079–1082. ISSN: 0028-0836. DOI: 10.1038/nature03805.

[78] A. H. Clark, L. Kondic, and R. P. Behringer. “Particle scale dynamics in granular impact”. In: *Physical Review Letters* 109.23 (Dec. 2012), p. 238302. ISSN: 00319007. DOI: 10.1103/PhysRevLett.109.238302. arXiv: arXiv:1208.5724v1.

[79] Scipy.org. *Scipy.signal.butter - http://tinyurl.com/scipy-butter*.

[80] H. Hertz and P. Lenard. *Gesammelte Werke von Heinrich Hertz, Band 4*. Ed. by A. Meiner and J. A. Barth. Vol. 4. Leipzig, 1895.

[81] A. T. Procopio, A. Zavaliangos, and J. C. Cunningham. “Analysis of the diametrical compression test and the applicability to plastically deforming materials”. en. In: *Journal of Materials Science* 38.17 (2003), pp. 3629–3639. ISSN: 00222461. DOI: 10.1023/A:1025681432260.

[82] D. W. Howell. “Stress distributions and fluctuations in static and quasi-static granular systems”. In: *Thesis (PhD). DUKE UNIVERSITY* (1999).

[83] A. J. Durelli and W. F. Riley. *Introduction to photomechanics*. Ed. by N. J. Englewood Cliffs. Prentice Hall, 1965, p. 402.

[84] Modlex3D. *Optics Theories - http://support.moldex3d.com/r13/moldex3d/module-introduction/standard-injection-molding/material/reference/optics-theories/*. 2016.

[85] M. M. Frocht. *Photoelasticity (vol. I & II)*. New York: John Wiley & Sons, 1941, p. 916. ISBN: 978-0-08-012998-3.

[86] T. S. Majmudar et al. "Jamming transition in granular systems". In: *Physical Review Letters* 98.5 (Feb. 2007), p. 058001. ISSN: 00319007. DOI: 10.1103/PhysRevLett.98.058001. arXiv: 0610645 [cond-mat].

[87] A. H. Clark et al. "Nonlinear force propagation during granular impact". In: *Physical Review Letters* 114.14 (Apr. 2015), p. 144502. ISSN: 10797114. DOI: 10.1103/PhysRevLett.114.144502. arXiv: 1408.1971.

[88] H. G. Matuttis, S. Luding, and H. J. Herrmann. "Discrete element simulations of dense packing and heaps made of spherical and non-spherical particles". In: *Powder Technology* 109.1-3 (1999), pp. 278–292. ISSN: 0032-5910.

[89] H. A. Khawaja and K. Parvez. "Validation of Normal and Frictional Contact Models of Spherical Bodies by Fem Analysis". en. In: *The International Journal of Multiphysics* (Aug. 2010). ISSN: 17509548. DOI: 10.1260/1750-9548.4.2.175.

[90] X. Jia, C. Caroli, and B. Velicky. "Ultrasound Propagation in Externally Stressed Granular Media". In: *Physical Review Letters* 82.9 (Mar. 1999), pp. 1863–1866. ISSN: 0031-9007. DOI: 10.1103/PhysRevLett.82.1863.

[91] A. Donev, S. Torquato, and F. H. Stillinger. "Pair correlation function characteristics of nearly jammed disordered and ordered hard-sphere packings". In: *Physical Review E - Statistical, Nonlinear, and Soft Matter Physics* 71.1 (Jan. 2005), p. 011105. ISSN: 15393755. DOI: 10.1103/PhysRevE.71.011105. arXiv: 0408550 [cond-mat].

[92] L. E. Silbert. "Jamming of frictional spheres and random loose packing". en. In: *Soft Matter* 6.13 (June 2010), p. 2918. ISSN: 1744-683X. DOI: 10.1039/c001973a.

[93] S. R. Hostler. "Wave propagation in granular materials". PhD thesis. California Institute of Technology, 2005, p. 111.

[94] S. Frank-Richter. "Disordered Binary Granular Packings in Three Dimensions". Phd Thesis. Heinrich-Heine-Universität Düsseldorf, May 2014, p. 133.